

# MMP-2-triggered, mitochondria-targeted PROTAC-PDT therapy of breast cancer and brain metastases inhibition

Received: 4 January 2024

Accepted: 19 November 2024

Published online: 29 November 2024

Fan Tong<sup>1</sup>, Yufan Wang<sup>1</sup>, Yanyan Xu<sup>1</sup>, Yang Zhou<sup>1,2</sup>, Siqin He<sup>1</sup>, Yufan Du<sup>1</sup>,  
Wenqin Yang<sup>1</sup>, Ting Lei<sup>1</sup>, Yujun Song<sup>1</sup>, Tao Gong<sup>1</sup> & Huile Gao<sup>1</sup>✉

Proteolytic targeting chimera (PROTAC) technology is a protein-blocking technique and induces antitumor effects, with potential advantages. However, its effect is limited by insufficient distribution and accumulation in tumors. Herein, a transformable nanomedicine (dBET6@CFMPD) with mitochondrial targeting capacity is designed and constructed to combine PROTAC with photodynamic therapy (PDT). In this work, we demonstrate that dBET6@CFMPD exhibits great biodistribution and retention, and can induce potent antitumor response to suppress primary and metastatic tumors, becoming a nanomedicine with potential in cancer combination therapy.

Proteolytic targeting chimera (PROTAC) technology is a protein-blocking technique based on ubiquitination-proteasome system (UPS) targeting that can induce protein degradation<sup>1,2</sup>. However, PROTAC agents generally display low water solubility, unfavorable pharmacokinetics, and lack tumor specificity<sup>3</sup>, leading to systemic toxicity<sup>4,5</sup>. Some reports have indicated that ligand modification (such as antibodies, folate, and aptamers) can achieve the tumor-targeted delivery of PROTAC<sup>6–8</sup>. However, these ligand-PROTAC conjugates suffer from complicated synthetic processes, heterogeneous expression of receptors, and limited tumor penetration, limiting the clinical translation and antitumor effects. Moreover, PROTAC generally targets and degrades a specific protein, which induces limited antitumor effects. Therefore, there is a great challenge and prospect to combine PROTAC with other antitumor therapies and achieve tumor-specific distribution of PROTAC<sup>9</sup>, via a simple and multifunctional nanoplatform.

Photodynamic therapy (PDT) is an antitumor therapy, consisting of a photosensitizer (PS) that produces reactive oxygen species (ROS) under laser irradiation to kill cancer cells<sup>10,11</sup>, and has been approved for clinical use in breast, lung, skin, and esophageal cancers as a typical treatment pattern<sup>12,13</sup>. Meanwhile, PDT also induces immunogenic cell death (ICD) of tumor cells and provokes anti-tumor immune responses<sup>14–16</sup>. However, it has been shown that programmed cell death ligand 1 (PD-L1, a main immunosuppressive factor) upregulation exists after PDT<sup>17–19</sup>. PD-L1 on the tumor membrane interacts with PD-1

on the surface of T cells, which in turn inhibits T cell proliferation and cytotoxicity and promotes immune escape, leading to tumor recurrence and metastasis<sup>20,21</sup>. Additionally, tumor-associated macrophages (TAMs), the major tumor-infiltrating immunosuppressive cells in the tumor immunosuppressive microenvironment (TIME), facilitate tumor growth and metastases<sup>22–24</sup>. Interestingly, BRD4 regulates PD-L1 expression by binding to its promoter transcriptionally and BRD4 inhibition reduces PD-L1 expression<sup>25,26</sup>. In addition, the lack of c-Myc in mice affects the maturation of TAMs, which may trigger TAMs repolarization to M1 phenotypes<sup>27</sup>. dBET6, a BRD4 degrader based on the PROTAC technology, can achieve effective and sustained degradation of BRD4 protein, thus exerting anti-tumor effects and immunomodulatory effects<sup>28–30</sup>. Therefore, dBET6 can remodel the TIME and synergistically inhibit tumor and metastatic progression with PDT, by down-regulating PD-L1, inhibiting c-Myc expression and repolarizing TAMs.

Although nanocarriers can improve the biodistribution of PROTAC and PS, the highly complex tumor microenvironment, such as dense stroma, higher solid stress, and high tissue fluid pressure, impedes the penetration and retention of nanomedicines within the tumor<sup>31,32</sup>. Notably, the permeability and retention of static nanoparticles are usually contradictory, i.e., large-sized nanoparticles have better retention ability and poor permeability, and vice versa for small-sized nanoparticles<sup>33,34</sup>. Numerous studies have shown that

<sup>1</sup>Key Laboratory of Drug Targeting and Drug Delivery Systems, West China School of Pharmacy, Sichuan University, Chengdu 610041, China. <sup>2</sup>Key Laboratory of Tropical Biological Resources of Ministry of Education, School of Pharmaceutical Sciences, Hainan University, Haikou 570200, China.

✉ e-mail: [gaohuile@scu.edu.cn](mailto:gaohuile@scu.edu.cn)

deformable nanoparticles hold promise for improving nanodrug permeability and retention<sup>34–36</sup>. Diphenylalanine with L-Phe-Phe structure, deriving from the pathogenesis of Alzheimer's disease, has been proposed to serve as a core recognition motif capable of guiding self-assembly to form functional nanostructures, such as nanofibers and nanowires<sup>37,38</sup>. Thus, the Phe-Phe-Arg-Phe-Lys (FFRFK) peptide, with a mitochondrial targeting ability<sup>39,40</sup>, can be used to construct in situ transformable nanocarriers for the delivery of PROTAC and PS to facilitate their penetration and accumulation. Meanwhile, following in situ deformation, the nanofibers can further target mitochondria to enhance PDT-induced oxidative stress. However, there has been no study to investigate the effect of nanofibers themselves on tumor cells. We envision that in situ-formed nanofibers target and accumulate in mitochondria, which in turn affects mitochondria or causes damage and promotes the apoptosis of tumor cells.

In this work, we construct a multifunctional PROTAC-PDT nano-platform (dBET6@CFMPD) to treat breast cancer and its metastasis. dBET6@CFMPD is obtained via the self-assembly between dBET6 and the photosensitizer chlorin e6 (Ce6)-modified MMP-2 (matrix metalloproteinase-2) sensitive peptide (FFRKGPLGLAGC)-PEG-DSPE conjugates (Fig. 1a). After accumulating in the tumor site, dBET6@CFMPD can respond to the high level of MMP-2 in the TME. The Ce6-FFRKGPLG fragment obtained by enzymatic cleavage can form nanofibers due to FF dipeptide, which will increase the accumulation of Ce6, further enhance the PDT effect, and induce a strong ICD effect. Then, the nanofibers target mitochondria and induce mitochondria damage to facilitate tumor cell death. Meanwhile, the released dBET6 can continuously degrade BRD4, induce apoptosis of tumor cells, down-regulate the expression of PD-L1, and repolarize TAMs, thus remodeling the TIME. In vitro and in vivo experiments demonstrated that dBET6@CFMPD can potently inhibit the progression of breast cancer and its metastases by PROTAC-PDT combination therapy and remodeling the TIME.

## Results

### Preparation and characterization of nanomedicines

The Ce6-conjugated chimeric molecules Ce6-PEG<sub>3400</sub>-DSPE (CPD), Ce6-FFRKGPLLAGC-PEG<sub>2000</sub>-DSPE (CFPD), and Ce6-FFRKGPLGLAGC-PEG<sub>2000</sub>-DSPE (CFMPD) were synthesized by using previous methods with minor modifications<sup>32</sup>. The peaks around 2218.10, 1412.87, 1412.59, 4275.26, and 4225.27 belonged to DSPE-PEG<sub>2000</sub>-Mal (Supplementary Fig. 1a), FFRKGPLLAGC (MMP-2 responsive peptide, Supplementary Fig. 1b), FFRKGPLLAGC (control peptide, Supplementary Fig. 1c), CFPD (Supplementary Fig. 1d), and CFMPD (Supplementary Fig. 1e), respectively. Compared to DSPE-PEG<sub>2000</sub>-Mal, the molecular weights of both CFPD and CFMPD increased by approximately 2000, which is exactly the sum of the molecular weights of the peptide sequence and Ce6, suggesting the successful conjugation of DSPE-PEG<sub>2000</sub>-Mal, Ce6, and control/MMP-2 responsive peptide. Similarly, CPD was synthesized successfully, due to the peaks of around 3402.44 and 4027.51, belonging to DSPE-PEG<sub>3400</sub>-NH<sub>2</sub> and CPD, respectively (Supplementary Fig. 1f, g). CPD, CFPD, and CFMPD could self-assemble to form nanoparticles, with similar sizes around 90 nm (Supplementary Fig. 1h–j). After dBET6 encapsulation, the average sizes of dBET6@CPD, dBET6@CFPD, and dBET6@CFMPD were  $85.7 \pm 3.0$  nm (PDI = 0.160),  $87.0 \pm 5.2$  nm (PDI = 0.221), and  $90.9 \pm 4.5$  nm (PDI = 0.196), respectively. The zeta potentials were  $-10.1 \pm 0.6$  mV,  $-10.1 \pm 0.2$  mV, and  $-8.6 \pm 0.1$  mV, respectively, measured by dynamic light scattering (DLS) analysis (Fig. 1b–d and Supplementary Fig. 1k). The transmission electron microscopy (TEM) images showed the spherical morphologies of dBET6@CPD, dBET6@CFPD, and dBET6@CFMPD (Fig. 1b–d).

The MMP-2 responsiveness of nanomedicines was investigated by multiple assays. Firstly, we measured the mass weight changes of CFPD and CFMPD after incubation with human MMP-2 to investigate the responsive disassembly. After incubation with MMP-2 for 4 and 24 h,

the CFPD group showed no significant change in molecular mass (Fig. 1e). The CFMPD group showed distinct new peaks belonging to the post-enzymatic fragmentation (Fig. 1f). The DLS data and TEM images investigated the responsive shape-transformation behaviors of nanomedicines. The size distribution of dBET6@CFMPD with MMP-2 was increased from 91.0 nm to 366.0 nm and the PDI was changed from 0.180 to 0.434 (Supplementary Fig. 1l). Meanwhile, the spherical morphology of dBET6@CFMPD transformed into larger nanofibers (Fig. 1g), while the morphology of dBET6@CFPD did not change (Supplementary Fig. 1m), suggesting that dBET6@CFMPD, but not dBET6@CFPD, was able to achieve the shape transformation in response to MMP-2. Moreover, the intracellular shape transformation was evaluated by TEM. The cells treated with dBET6@CFMPD + MMP-2 exhibited nanofibers in the cytoplasm. Spherical nanoparticles and no nanofibers were in cells incubated with dBET6@CFPD + MMP-2 (Fig. 1h, i). These results jointly indicated the MMP-2 responsivity and shape transformation of dBET6@CFMPD.

### Cellular uptake and retention in vitro

Flow cytometry and confocal imaging were carried out to investigate nanomedicines' cellular uptake and retention. The confocal images showed that FFRFK modification could promote the uptake of Ce6 in 4T1 cells, and MMP-2 responsive shape transformation further motivated the cellular uptake (Fig. 2a). Then the nanomedicines were pre-treated with MMP-2 for 12 h to form nanofibers. After incubation for 1, 2 and 4 h, the CFMPD group showed enhanced uptake in 4T1 cells, compared with free Ce6, CPD, and CFPD groups (Fig. 2b). Similar results were obtained by flow cytometry. CFPD and CFMPD groups showed 5.71-fold and 6.53-fold stronger fluorescence signals than free Ce6 at 1 h, while 3.73-fold and 4.13-fold higher at 4 h, and 3.10-fold and 3.64-fold stronger at 12 h, respectively (Fig. 2c). Moreover, CFMPD exhibited more fluorescence signals than CFPD, resulting from the responsive shape switch. After being pre-treated with MMP-2, CFPD also showed the strongest uptake, followed by CFPD, benefiting from the modification of mitochondria-targeting ligand FFRFK, and MMP-2 triggered shape transformation (Fig. 2d).

The retention of nanomedicine was evaluated by confocal imaging of multicellular spheroids (MSCs). After 12 h incubation, the medium containing different formulations was replaced with fresh serum-free medium and the MSCs were cultured for another 12 h. Free Ce6 was excreted rapidly, with vanishing fluorescence signals at 80  $\mu$ m. CPD, CFPD, and CFMPD distributed more than 80  $\mu$ m of z-axis in MSCs, showing good penetration ability, benefiting from the small size of nanomedicines. However, CPD and CFPD were excreted rapidly, tending to vanish at 100  $\mu$ m. CFMPD displayed strong retention in MSCs, with high fluorescent intensity even at 100 and 120  $\mu$ m, resulting from MMP-triggered shape transformation and nanofiber formation (Fig. 2e, f). These results jointly illustrated that spherical CFMPD could penetrate deeply into tumors and motivate the cellular uptake of the photosensitizer. After the reaction with MMP-2, the nanomedicines transformed from spherical nanoparticles to nanofibers, increasing the retention and improving PDT efficiency.

### Mitochondrial localization and mitochondrial damage

The peptide sequence of FFRFK endowed nanomedicines with mitochondria-targeting capabilities, which were investigated through confocal microscopy. A mitochondrial-specific dye, mito-tracker, was utilized to perform colocalization studies of CFMPD. After incubation for 1 h, CFMPD pre-incubated with MMP-2 (CFMPD + MMP-2) showed the most fluorescence of Ce6 in mitochondria, followed by CFMPD and CFPD, benefiting from FFRFK exposure induced by MMP-2 enzymatic reaction (Supplementary Fig. 2a). With an increase of time, at 4 h, FFRFK-containing formulations were present in mitochondria at a different degree, indicating the targeting capacity of the peptide sequence (Fig. 2g). Similarly, MMP-2-pretreated CFMPD showed the best co-

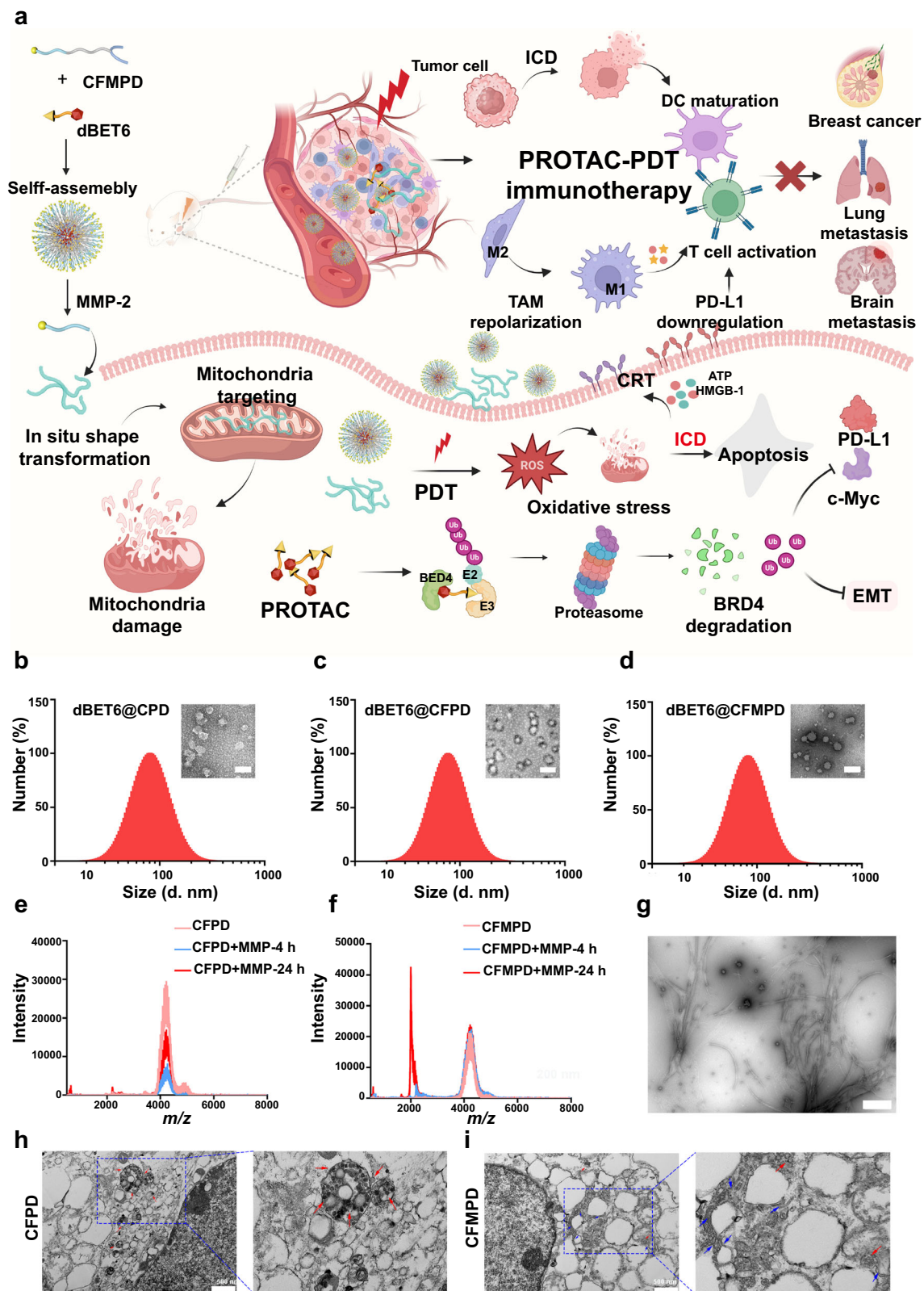


**Fig. 1 | Preparation and characterization of nanomedicines.** **a** Schematic illustration of the composition of dBET6@CFMPD and its therapeutic effect on primary breast cancer and brain metastases. **a** Created with BioRender.com released under a Creative Commons Attribution-NonCommercial-NoDerivs 4.0 International license. The DLS results and TEM images of **b** dBET6@CPD, **c** dBET6@CFPD, and **d** dBET6@CFMPD (scale bar = 200 nm). The molecular mass changes of CFPD (**e**) and CFMPD (**f**) after incubation with MMP-2 for 4 and 24 h were detected by MALDI-

TOF-MS analyses. MALDI-TOF-MS spectra of **e**, **f** are included in Supplementary Figs. 10 and 11. **g** The TEM images of dBET6@CFMPD after incubation with MMP-2 (scale bar = 2 μm). The TEM images and enlarged images of cells treated with CFPD (**h**) and CFMPD (**i**). Red arrows and blue arrows indicate spherical nanoparticles and nanofibers, respectively (scale bar = 500 nm). Source data are provided as a Source Data file.



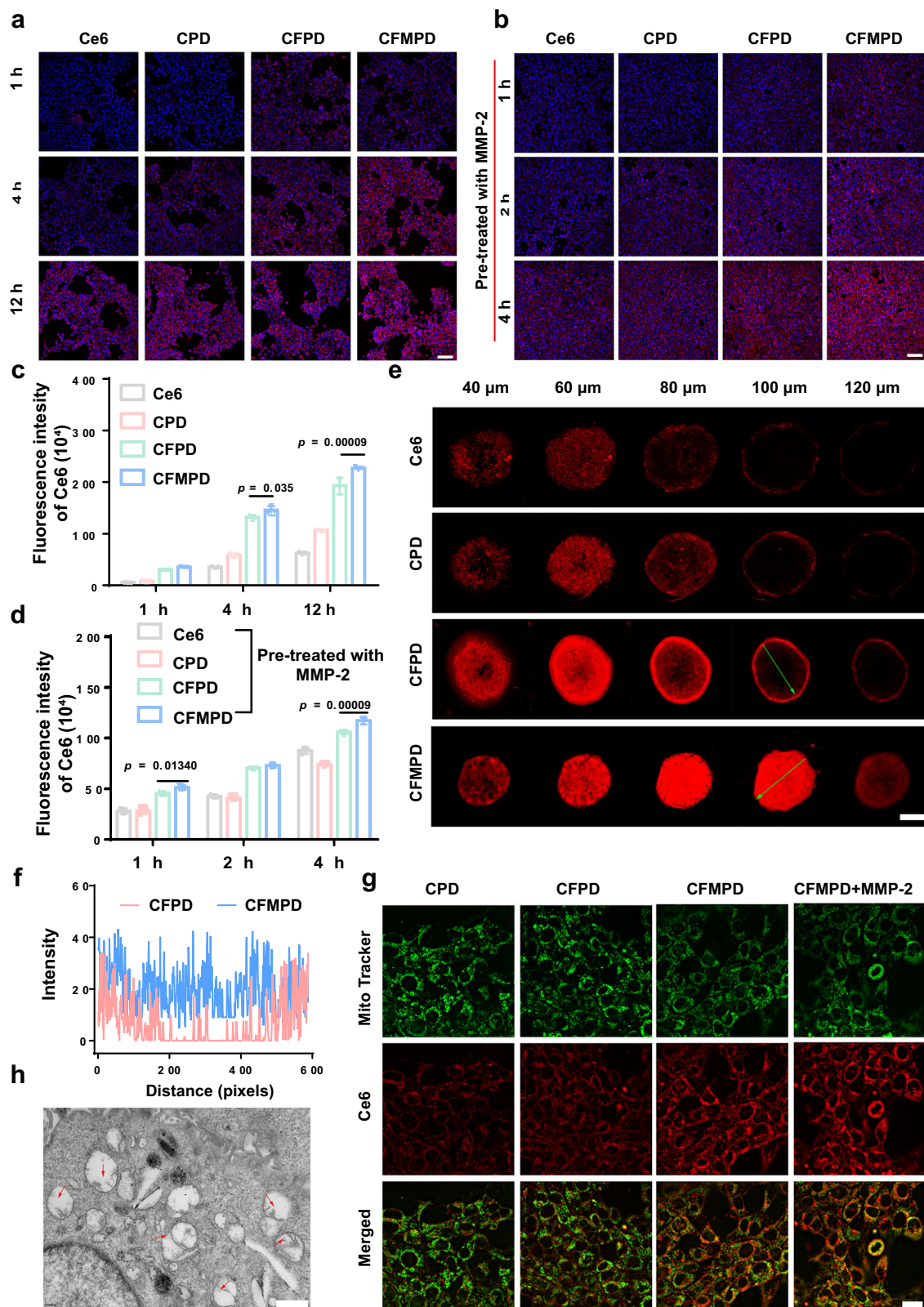


**Fig. 2 | Cellular uptake, retention, and mitochondria targeting. a, b** Cellular uptake assay of different formulations by fluorescence microscope (scale bar = 100  $\mu$ m). **c, d** Cellular uptake assay of different formulations by flow cytometry ( $n = 3$  independent cell lines). **e** Confocal images of 4T1 MSCs incubated with free Ce6, CPD, CFPD, and CFMPD for 12 h (scale bar = 100  $\mu$ m). **f** Quantitative analyses of tumor spheroid sections at 100  $\mu$ m. **g** Mitochondrial localization analyses of different formulations in 4T1 cells (scale bar = 20  $\mu$ m). **h** TEM image of cells treated

with CFMPD (scale bar = 1  $\mu$ m). Red arrows indicate mitochondrial cristae. All data are presented as mean  $\pm$  SD. Two-tailed Student's *t* test and One-way analysis of variance (ANOVA) with a Tukey post hoc test were used for the statistical comparison between the two groups and among multiple groups, respectively. A significant difference was considered when the *p* value was  $<0.05$ . Source data are provided as a Source Data file.



localization in mitochondria, and CFMPD displayed more red fluorescence in mitochondria, due to the increased uptake. These results confirmed the mitochondria-targeting functions of CFMPD, benefiting from the sequence of FFRFK, which was enhanced by enzyme-triggered shape transformation and exposure of FFRFK sequence.

Then, the effects of nanomedicines on mitochondria were further studied. We observed the mitochondria morphology by TEM, after incubation with different formulations for 12 h. Briefly, the mitochondria in cells treated by medium (as control) and CPD displayed normal matrix electron density and cristae (Supplementary Fig. 2b, c). And CFPD group showed normal electron density and short cristae (Supplementary Fig. 2d), suggesting slight mitochondrial damage. The mitochondrial matrix was swollen, cristae were short and disorganized, and matrix electron density was significantly decreased in the CFMPD group, indicating heavy mitochondrial damage (Fig. 2h). The decreased mitochondrial membrane potential is another important marker of mitochondrial damage, which was detected by JC-1 assay. There were increased JC-1 monomers and reduced JC-1 aggregates in cells incubated with CFMPD with/without MMP-2, suggesting strong mitochondrial damage even at a low concentration (Supplementary Fig. 2e, f). All the results demonstrated that CFMPD could accumulate in the mitochondria and induce mitochondrial damage in tumor cells, due to the mitochondria targeting capacity and transformable shape.

### BRD4 degradation and c-Myc downregulation

BRD4, a member of the BET protein family, is largely acknowledged in cancer for its role in super-enhancers (SEs) organization and oncogenes expression regulation<sup>41</sup>. The silencing of BRD4 shortcuts the communication between SEs and target promoters with subsequent cell-specific repression of oncogenes to which cancer cells are addicted and cell apoptosis. The BRD4 degradation capacity of free dBET6 was assessed with western blot analysis. As Supplementary Fig. 2g showed, dBET6 degraded the overexpressed BRD4 proteins in a concentration-dependent manner, inducing the subsequent downregulation of downstream c-Myc. Meanwhile, we also measured the degradation efficiency of dBET6 after self-assembly with CPD, CFPD, and CFMPD. The dBET6-containing formulations heavily degraded BRD4 and downregulated c-Myc, suggesting no negative effect on BRD4 degradation of dBET6 after encapsulation (Fig. 3a). As a downstream effector of BRD4, c-Myc eventually promotes tumor cell apoptosis. Therefore, dBET6 could degrade BRD4 proteins and downregulate downstream proteins associated with tumor oncogenes, which synergized with PDT to suppress tumor progress.

### Inhibition of PD-L1

The inhibition of dBET6 on PD-L1 expression was investigated using flow cytometry and immunofluorescence staining. 4T1 cells were pre-treated with interferon- $\gamma$  (IFN- $\gamma$ ) to stimulate PD-L1 expression and then treated with different formulations. The results indicated that PDT could induce upregulation of PD-L1, which was downregulated by BRD4 degradation to the normal level (Fig. 3b). The dBET6@CFMPD treated cells exhibited a 2.53-fold lower PD-L1 level than the CFMPD+L group, whose PDT efficiency was improved by transformable shape-enhanced uptake and retention. Moreover, even in a low concentration (0.25  $\mu\text{g/mL}$ ), dBET6 still exhibited inhibitory effect on PD-L1 expression. The results of immunofluorescence staining were well consistent with the results mentioned above, intuitively displaying the PD-L1 downregulation (Supplementary Fig. 2h). The results verified that PD-L1 was upregulated after PDT and could be further downregulated by BRD4 inhibitor.

### ROS generation

Intracellular ROS levels of 4T1 cells treated with different formulations were investigated by flow cytometry, using a ROS probe (DCFH-DA). Upon 650 nm laser irradiation, high green fluorescent signals were

observed in cells treated with PDT, including Ce6+L, CPD+L, CFPD+L, and CFMPD+L. With the addition of dBET6 to PDT, ROS generation was reduced, probably due to the pro-apoptosis effect of dBET6 itself, resulting in a decrease in cell viability and number. CFMPD+L treatment showed the highest ROS generation, which benefited from the increased cellular uptake and shape transformation-enhanced retention (Fig. 3c). Consistent with this result, the ROS-generating capacity of the dBET6@CFMPD group was much better than that of the dBET6@CPD and dBET6@CFPD groups. These data verified that CFMPD with changeable shapes could promote ROS generation and PDT efficiency, inducing ablation of tumor cells.

### Antitumor effect in vitro

Encouraged by shape-transformation capacity, ROS generation, and BRD4 degradation, the antitumor effect at the cellular level was investigated, by employing various methods. Firstly, the MTT assay was carried out to investigate further the relationship between formulation concentration and cytotoxicity in tumor cells (4T1, E0771 cells) and normal cells (RAW264.7 cells). The cytotoxicity of free dBET6 on 4T1 and RAW264.7 cells was evaluated. There was obvious cell toxicity caused by concentrated dBET6 in tumor cells and normal cells, due to the apoptosis induced by BRD4 degradation and c-Myc inhibition (Supplementary Fig. 3a, b). There was negligible cytotoxicity in RAW 264.7 cells treated with CPD, CFPD, and CFMPD (Supplementary Fig. 3c), while a potent killing effect was induced upon laser irradiation in 4T1 cells (Fig. 3d). CFMPD+L induced most tumor cell apoptosis compared with free Ce6, CPD, and CFPD. Meanwhile, dBET6-loaded nanomedicines with high concentrations could trigger tumor cell death, which was enhanced strongly by laser irradiation (Fig. 3e), confirming the practicability of combinational therapy. 4T1 cells treated with dBET6@CFMPD+L were heavily killed, and only a relative 12.81% cell viability was detected at a Ce6 concentration of 5  $\mu\text{g/mL}$ . The in vitro antitumor effect of nanomedicines was also carried out on E0771 cells (Supplementary Fig. 3d, e). The results were well consistent with the MTT assay on 4T1 cells. PDT could induce strong cytotoxicity on tumor cells, which was further improved by transformable shape and BRD4 degradation (Supplementary Table 1).

The results of apoptosis analyses were well consistent with the outcomes of MTT assays. dBET6@CFMPD+L treatment induced the highest apoptosis rate, compared with other groups, resulting from the combination of BRD4 degradation and retention-enhanced PDT triggered by MMP-2 responsive shape transformation (Fig. 3f, g). The calcein-AM/PI double staining was also carried out to evaluate the antitumor effect in vitro. Similarly, the combination of BRD4 inhibitor and PDT induced heavy death of tumor cells, observed by high PI fluorescence signals (Fig. 3h). In a nutshell, dBET6@CFMPD realized strong cytotoxicity when receiving irradiation, compared to parent CFMPD nanoparticles and dBET6@CFPD. These results proved that the strategy of retention enhancement and combinational therapy has potential for potent antitumor therapy.

### ICD in vitro

Exposure of calreticulin (CRT), release of ATP and high mobility group protein 1 (HMGB-1) were measured to investigate the ICD effect. The cells treated with dBET6@CFMPD+L translocated more CRT on the cell surface than other groups, displaying 1.25-fold higher CRT fluorescence than CFMPD+L-treated cells while 1.29-fold higher than dBET6@CFPD+L, respectively (Fig. 4a, b). Similarly, combinational therapy induced more ATP and HMGB-1 release than single PDT treatment (Fig. 4c, d), which was facilitated by shape transformation-enhanced intracellular uptake and retention. These results suggested that dBET6 could promote PDT to induce potent ICD efficiency, further maturing DCs and triggering an antitumor immune response.

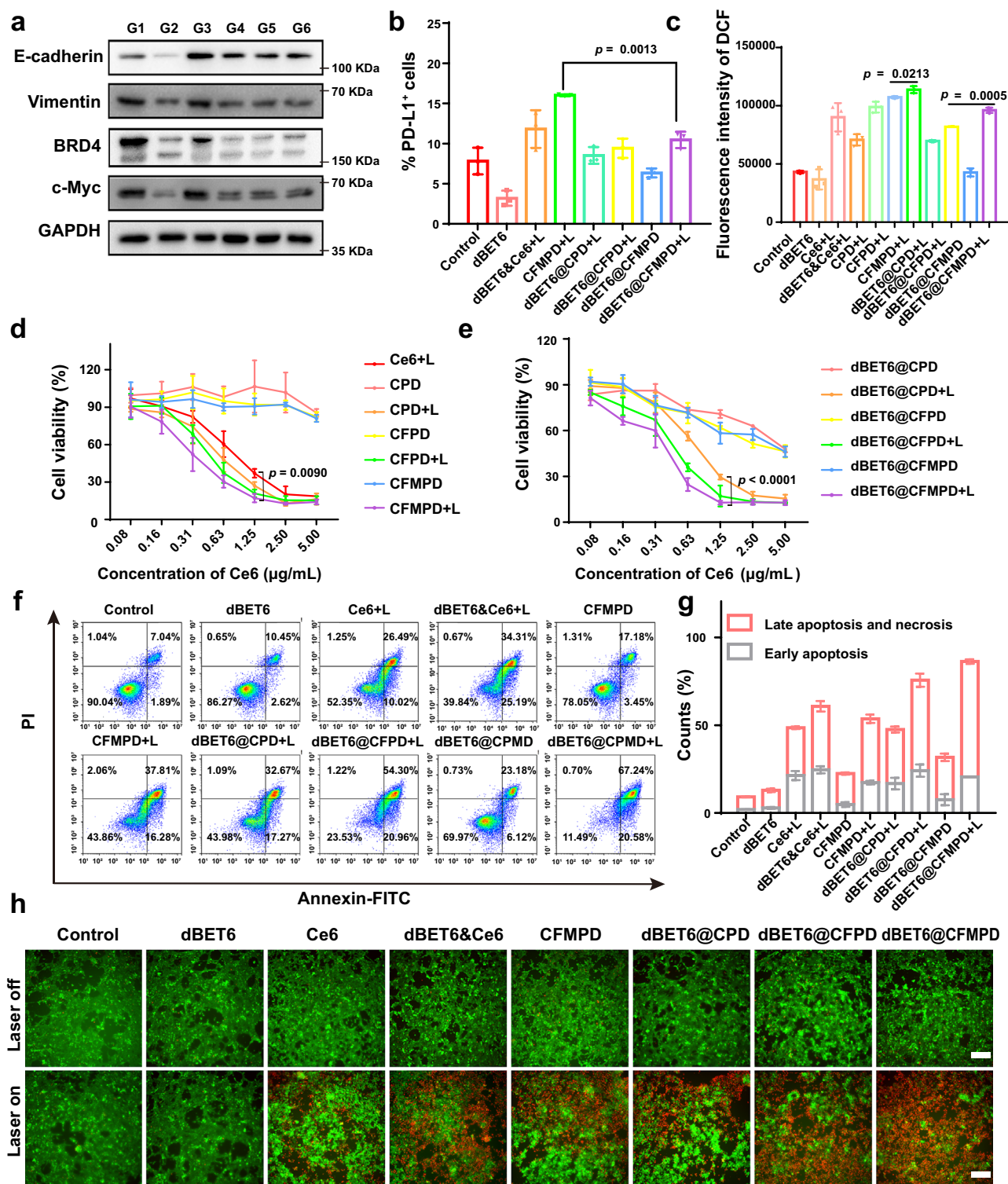


**Fig. 3 | BRD4 inhibition and antitumor effect in vitro.** **a** WB analyses of BRD4 inhibition and EMT downregulation on 4T1 cells. The G1-G6 represent control, dBET6&Ce6+L, CFMPD+L, dBET6@CPD+L, dBET6@CFPD+L, and dBET6@CFMPD+L, respectively. **b** PD-L1 expression of 4T1 cells treated with different formulations. **c** Detection of intracellular ROS generation by flow cytometry ( $n = 3$  independent experimental cell lines). MTT assay after incubating 4T1 cells with parent nanoparticles (**d**) and BET6-loaded nanoparticles (**e**).  $n = 3$  independent cell lines. **f** Apoptosis assay of 4T1 cells treated with various formulations.

**g** Statistical results of apoptosis analysis ( $n = 3$  independent cell lines). **h** Live/dead double staining of 4T1 cells incubated with different preparations (scale bar = 100 μm). All data are presented as mean  $\pm$  SD. Two-tailed Student's  $t$  test and One-way analysis of variance (ANOVA) with a Tukey post hoc test were used for the statistical comparison between the two groups and among multiple groups, respectively. A significant difference was considered when the  $p$  value was  $< 0.05$ . Source data are provided as a Source Data file.



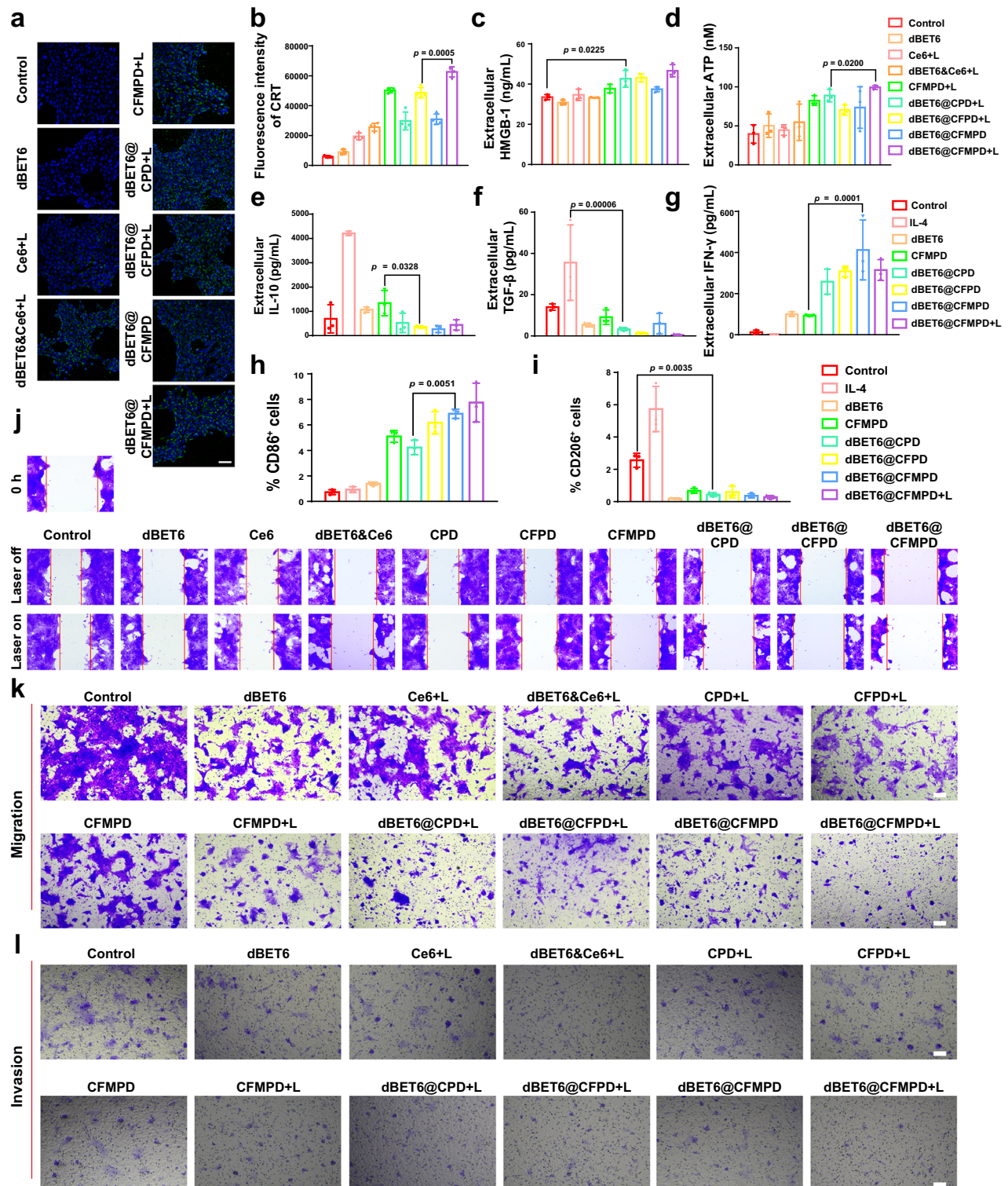


**Fig. 4 | Evaluation of ICD, macrophage polarization, and anti-metastasis effect.** **a, b** CRT exposure on the 4T1 cell surface was detected by confocal microscope and flow cytometry (scale bar = 50 μm,  $n = 3$  independent cell lines). **c, d** Extracellular HMGB-1 and ATP levels of tumor cells after incubation with different formulations ( $n = 3$  independent cell lines). **e–g** Secreted IL-10, TGF-β, and IFN-γ by RAW264.7 cells after treatment with different formulations ( $n = 3$  independent cell lines). **h, i** Flow cytometry analysis of the abundance of CD86<sup>+</sup> and CD206<sup>+</sup> RAW264.7 cells after

incubation with various formulations ( $n = 3$  independent cell lines). **j–l** Microscopy images of wound healing assay, migration assay, and invasion analysis of 4T1 cells treated with different formulations (scale bar = 100 μm). All data are presented as mean ± SD. Two-tailed Student's *t* test and One-way analysis of variance (ANOVA) with a Tukey post hoc test were used for the statistical comparison between the two groups and among multiple groups, respectively. A significant difference was considered when the *p* value was < 0.05. Source data are provided as a Source Data file.



## Macrophage repolarization

It has been known that BRD4 is revealed to participate in macrophages' inflammatory response and activate TAMs to exert pro-tumor effects. There have been reports to verify the capacity of BRD4 inhibitors to repolarize TAMs. Further experiment was carried out to investigate the macrophage repolarization effect of dBET6. According to the results of the MTT assay in RAW264.7 cells, we selected 0.25 µg/mL of dBET6 for subsequent experiments, with no influence on cell viability. The RAW 264.7 cells were treated with different formulations for 24 h after IL-4 pre-treatment for 12 h. Generally, different treatments containing dBET6 improved the secretion of IFN-γ, a biomarker of M1 macrophages, while there was an obvious decrease in IL-10 and TGF-β secretion, suggesting depressed M2 macrophages (Fig. 4e–g). The potential of BRD4 degradation for M2-to-M1 repolarization *in vitro* was further confirmed by flow cytometry analyses and fluorescent microscope. As shown in Fig. 4h, i and Supplementary Fig. 3f, dBET6 treatment could heavily increase the ratio of M1 cells (CD86<sup>+</sup> cells) and downregulate the percentage of M2 cells (CD206<sup>+</sup> cells). Moreover, dBET6@CFMPD showed stronger repolarization than dBET6@CFPD, which may be due to better cellular uptake and retention. Briefly, dBET6@CFMPD showed great potential for remodeling TIME, through PD-L1 downregulation and TAM repolarization.

## Anti-metastasis effect *in vitro*

The anti-metastasis effect and its mechanism were investigated through wound healing study, transwell assay, and WB analyses. As shown by Fig. 4j, BRD4 inhibition and PDT could retard the wound healing rate. The combination of BRD4 inhibitor and Ce6 suppressed cell migration strongly (Supplementary Fig. 3g). dBET6@CFMPD + L group displayed the lowest cell mobility (13.5%), followed by dBET6@CFPD + L (17.7%) and dBET6@CPD + L groups (17.7%). It was worth noting that the CFMPD restrained significantly cell migration, which reduced cell motility to 37.0%. Similar results were attained from migration and invasion experiments (Fig. 4k, l and Supplementary Fig. 3h, i). dBET6@CFMPD + L treatment induced the lowest migrated and invasive cells, showing 48.9% of migrated cells and 50.9% of invasive cells, which was much lower than CFMPD + L (66.1%, 64.3%), dBET6@CFMPD (52.6%, 61.4%), and dBET6@CFPD + L (52.6%, 69.0%). Moreover, CFMPD treatment also exhibited anti-metastasis according to migration and invasion assays. These data confirmed that nanomedicines with BRD4 degradation and transformable shape had a great capacity to suppress migration and invasion of tumor cells. On the other hand, WB analyses of cells treated with different formulations showed that nanomedicines containing dBET6 could downregulate vimentin and upregulate E-cadherin (Fig. 2a), indicating a decrease in endothelial mesenchymal transition (EMT). Therefore, the enhanced anti-metastasis effect of dBET6@CFMPD may benefit from (1) BRD4 degradation-induced downregulation of EMT<sup>42</sup>; (2) MMP-2 triggered shape conversion to nanofibers to restrict the movement of tumor cells, which was similar to the extracellular matrix; (3) PDT-induced decrease of cell viability and motivity.

## Biodistribution and retention

Encouraged by the shape conversion and retention in MSCs, CFMPD was further evaluated on animal models. Biodistribution and retention *in vivo* were observed by the IVIS Lumina imaging system after intravenous injection and intra-tumoral administration, respectively. As for the distribution study, free Ce6, as the control, was heavily distributed in the abdomen at 4 h and tended to vanish at 8 h post intravenous injection, indicating rapid elimination (Fig. 5a). CPD exhibited similar accumulation in the abdomen but distribution in the tumor at the early time point, compared to free Ce6. CFMPD showed the strongest accumulation in the tumor at all time points, compared with other groups, and stronger fluorescence signals in the tumor than in other

organs, suggesting specific tumor accumulation. The results of *ex vivo* imaging and confocal imaging of sections were consistent with that of *in vivo* imaging (Supplementary Fig. 4a, b). There were strong fluorescence signals in the livers and kidneys, suggesting that the liver and kidneys were the main metabolism organs of nanomedicines. However, the CFMPD group displayed the best accumulation in tumors, whose fluorescent signals were 1.22-fold and 1.71-fold higher than CFPD and CPD respectively (Fig. 5b, c). Confocal images of tumor sections also demonstrated the accumulation and penetration of CFMPD in tumors (Supplementary Fig. 4c). The data systematically confirmed that MMP-2 specific stimulation transformed CFMPD distributed in tumor sites from nanoparticles to nanofibers, which enhanced the retention and accumulation by preventing CFMPD pumped out from the tumor to the bloodstream.

As for retention assay, mice bearing with 4T1 tumor were intra-tumorally injected with CFPD and CFMPD and the *in vivo* images were obtained. Both CFPD and CFMPD showed almost equal fluorescence intensity at 5 min postinjection, suggesting an equal dose of formulations. CFPD tended to vanish in the tumor by 12 h post-injection. CFMPD showed greater accumulation and retention in tumors than CFPD after intra-tumoral injection, due to MMP-2 responsive formation of nanofibers (Fig. 5d). At 48 h post-injection, *ex vivo* images of tumors also verified the better retention of CFMPD in tumors (Fig. 5e), whose fluorescence intensity was 1.72-fold stronger than that of CFPD, according to the semi-quantification results and confocal images of sectioned tumors (Fig. 5f, g). To verify the shape conversion, TEM images of the tumor sections were observed (Supplementary Fig. 4d). The TEM images displayed that CFPD remained spherical with a size smaller than 100 nm, while there were nanofiber-like structures with elongated shapes surrounding tumor cells in CFMPD group. These results jointly demonstrated that CFMPD could be distributed in tumors and retained in tumors due to conversable shape triggered by MMP-2 in tumors.

## Evaluation of brain-targeting ability

Blood-brain barrier (BBB) penetration is one of the pivotal indices of nanodrugs in brain metastasis therapy. To substantiate the BBB permeability of the nanomedicines, we established a normal *in vitro* BBB model by seeding bEnd.3 cells in the upper chamber and 4T1 cells in the lower chamber (Fig. 6a). After administration for 4 h, the fluorescence intensity of solution in the lower chamber and nanoparticles taken by 4T1 cells was evaluated, revealing that CFMPD exhibited maximal content (Fig. 6b, c). Meanwhile, the confocal images also showed the highest penetration in bEnd.3 monolayer was observed in the CFMPD group, followed by CFPD and Ce6 groups (Supplementary Fig. 4e). Then, brain metastasis models were constructed to investigate the biodistribution and brain accumulation of nanoparticles *in vivo*. Notably, at 1, 2, 4, and 8 h post-injection, the fluorescence signals of CFMPD in the brain were much higher than in other groups (Fig. 6d), which was equipped with transformable shape and mitochondria targeting. At 8 h post-administration, the mice were sacrificed and major organs and brains were collected to obtain *ex vivo* images. There were fluorescence signals accumulated in the lung tissues of mice in the CPD and CFPD groups (Fig. 6e, g), which might be beneficial for suppressing lung metastasis. Meanwhile, there were more fluorescence signals in the livers and kidneys of mice treated with CPD and CFPD, compared to CFMPD group. However, there was much more fluorescence intensity in the brains of the CFMPD group than in other groups (Fig. 6f, h), whose signals were 2.43-fold, 2.04-fold, and 1.46-fold stronger than Ce6, CPD, and CFPD, respectively. These results jointly demonstrated that the nanomedicine containing the mitochondrial targeting peptide and responsively transformable shape could penetrate BBB and accumulate in the brain to realize the anti-metastasis effect.

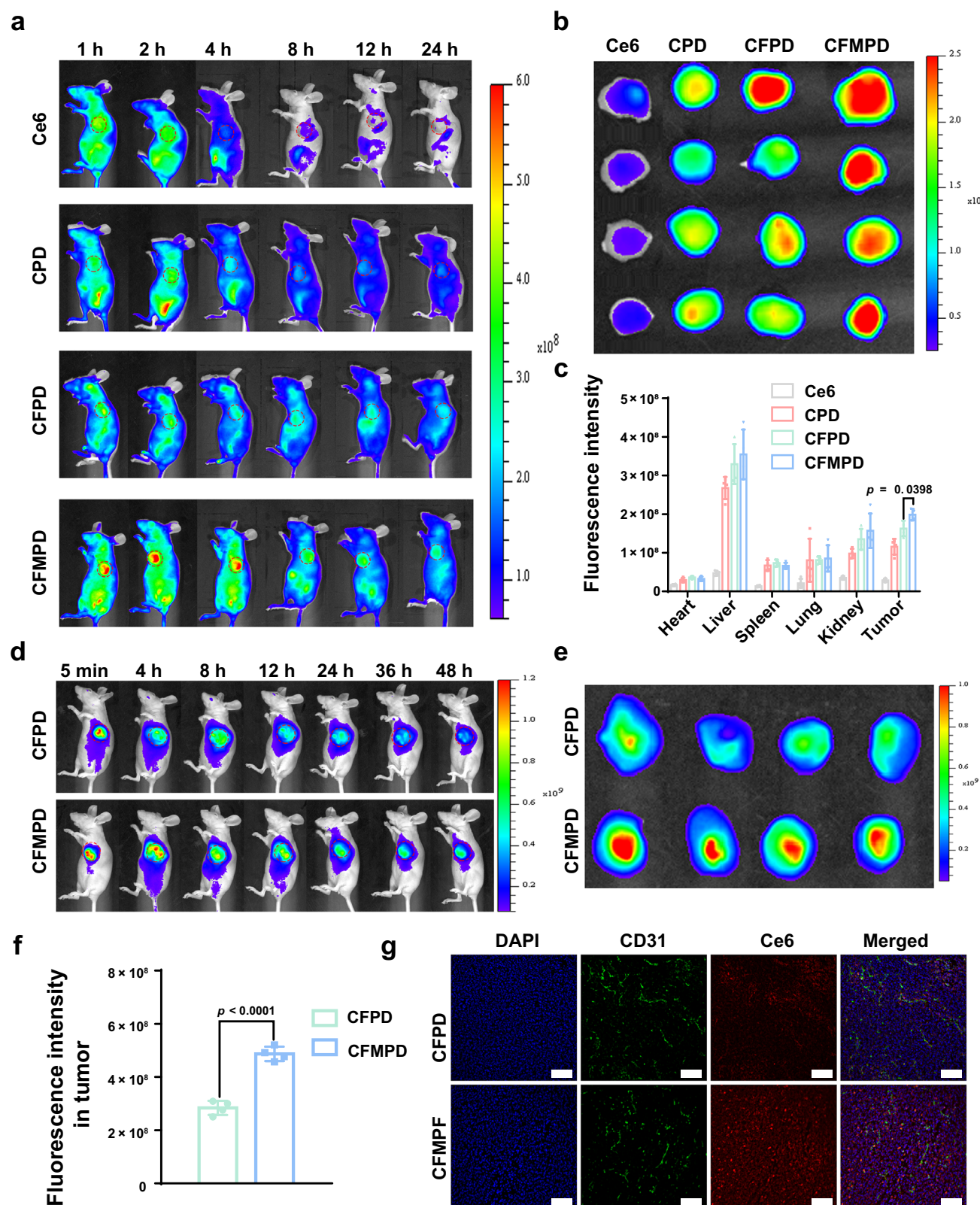


**Fig. 5 | In vivo targeting efficiency and retention effect of nanomedicines. a** In vivo imaging of mice at 1, 2, 4, 8, 12, 24 h post intravenous injection. **b** Ex vivo imaging of tumors. **c** Semi-quantification of major organs and tumors at 24 h post intravenous injection ( $n = 4$  mice). **d** In vivo fluorescent imaging of mice at 5 min, 4, 8, 12, 24, 36, and 48 h post intra-tumoral injection. **e** Ex vivo imaging of tumors at 48 h. **f** Semi-quantification of tumors ( $n = 4$  mice). **g** Fluorescent distribution of

frozen sections of tumors (scale bar = 100  $\mu\text{m}$ ). All data are presented as mean  $\pm$  SD. Two-tailed Student's  $t$  test and One-way analysis of variance (ANOVA) with a Tukey post hoc test were used for the statistical comparison between the two groups and among multiple groups, respectively. A significant difference was considered when the  $p$  value was  $< 0.05$ . Source data are provided as a Source Data file.



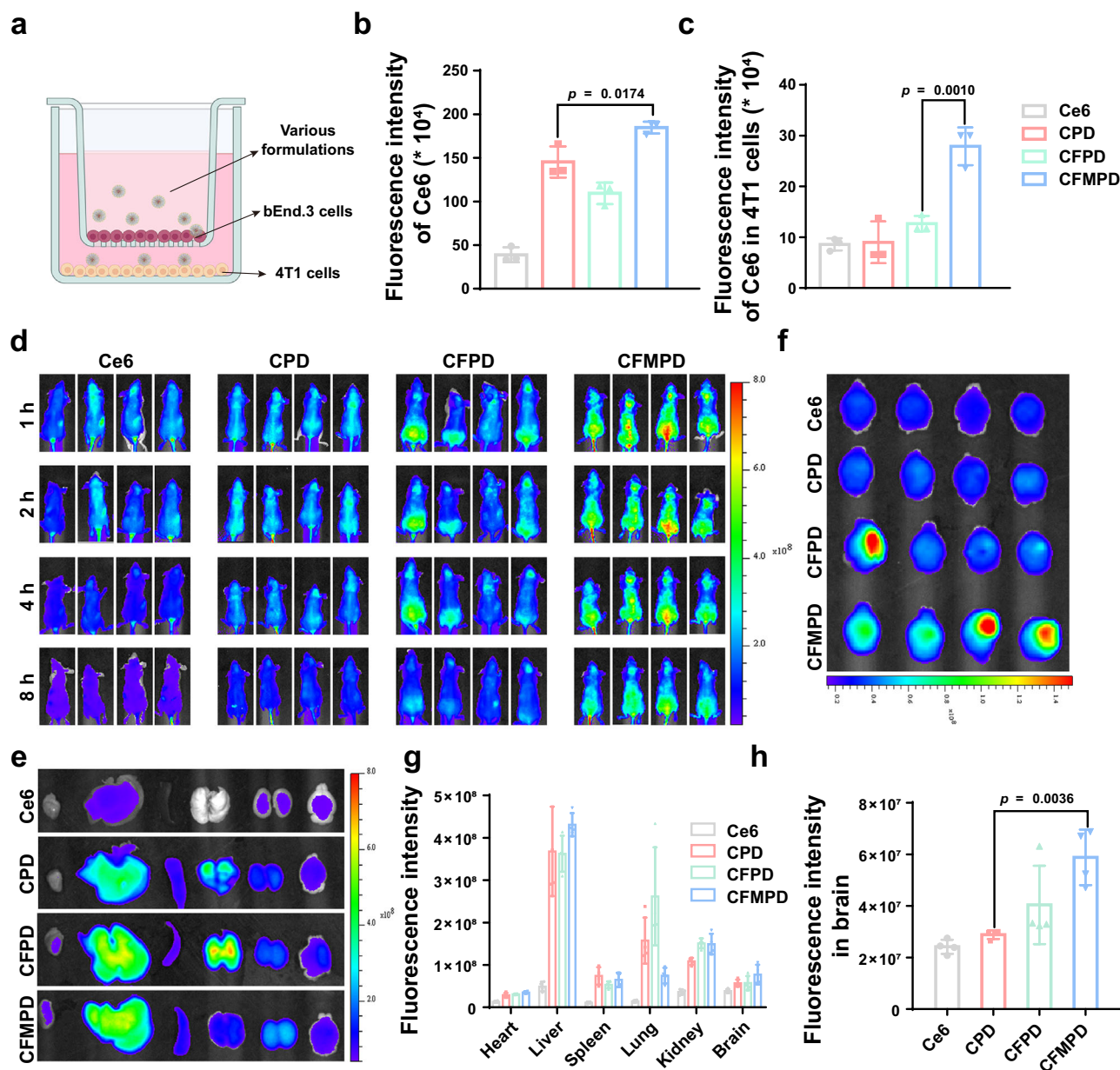


**Fig. 6 | Evaluation of brain-targeting ability.** **a** Schematic representation of the in vitro construction process for blood-brain barrier (BBB) and the traversal of BBB. Figure 1a Created with BioRender.com released under a Creative Commons Attribution-NonCommercial-NoDerivs 4.0 International license. **b** Fluorescence intensity of the supernatant liquid in the lower chamber after the introduction of NPs for 4 h ( $n = 3$  independent experimental units). **c** Fluorescence intensity of nanoparticles taken up by 4T1 cells in the lower chamber ( $n = 3$  independent cell lines). **d** In vivo imaging of mice bearing with brain-metastatic tumor at 1, 2, 4, 8 h

post intravenous injection. **e**, **f** Ex vivo imaging of major organs and brains at 8 h post intravenous injection. **g**, **h** Semi-quantification of major organs and brains ( $n = 4$  mice). All data are presented as mean  $\pm$  SD. Two-tailed Student's  $t$  test and One-way analysis of variance (ANOVA) with a Tukey post hoc test were used for the statistical comparison between the two groups and among multiple groups, respectively. A significant difference was considered when the  $p$  value was  $< 0.05$ . Source data are provided as a Source Data file.

### Antitumor and anti-metastasis in vivo

Inspired by promising cytotoxicity, high tumor selectivity, and great retention, the inhibition of tumor growth was evaluated on 4T1-subcutaneous mice models. The mice bearing breast cancer were divided into eight groups randomly, including Control, Ce6 + L, dBET6, CFMPD + L, dBET6@CFMPD, dBET6@CPD + L, dBET6@CFPD + L, and dBET6@CFMPD + L. CFMPD + L and dBET6@CPD + L groups displayed similar growth curves, much flatter than the Control group (Fig. 7a). The average tumor volume in the CFMPD + L group was around 400 mm<sup>3</sup>, but the dBET6@CFMPD + L group exhibited a much smaller volume (less than 200 mm<sup>3</sup>), indicating the combinational therapy efficiency of PROTAC and PDT. Meanwhile, the dBET6@CFMPD + L

group displayed the best antitumor effect, whose tumor suppression rate was 72.9%, followed by the dBET6@CFPD + L (55.4%) and dBET6@CPD + L (39.4%) groups. After 18-day treatment, the primary tumors were removed by surgery and collected for further investigation. The tumor weights (Fig. 7b) and ex vivo image of tumors (Supplementary Fig. 6a) also displayed similar results to the measurements of tumors in vivo. The data on tumor weights also showed that dBET6@CFMPD + L treatment induced the highest tumor suppression, corresponding to the results of the ex vivo tumor image. The body weights of mice in all groups slightly increased at the end of treatments (Fig. 7c). Hematoxylin & eosin (H&E) staining images showed no obvious histological changes in major organs, suggesting no significant



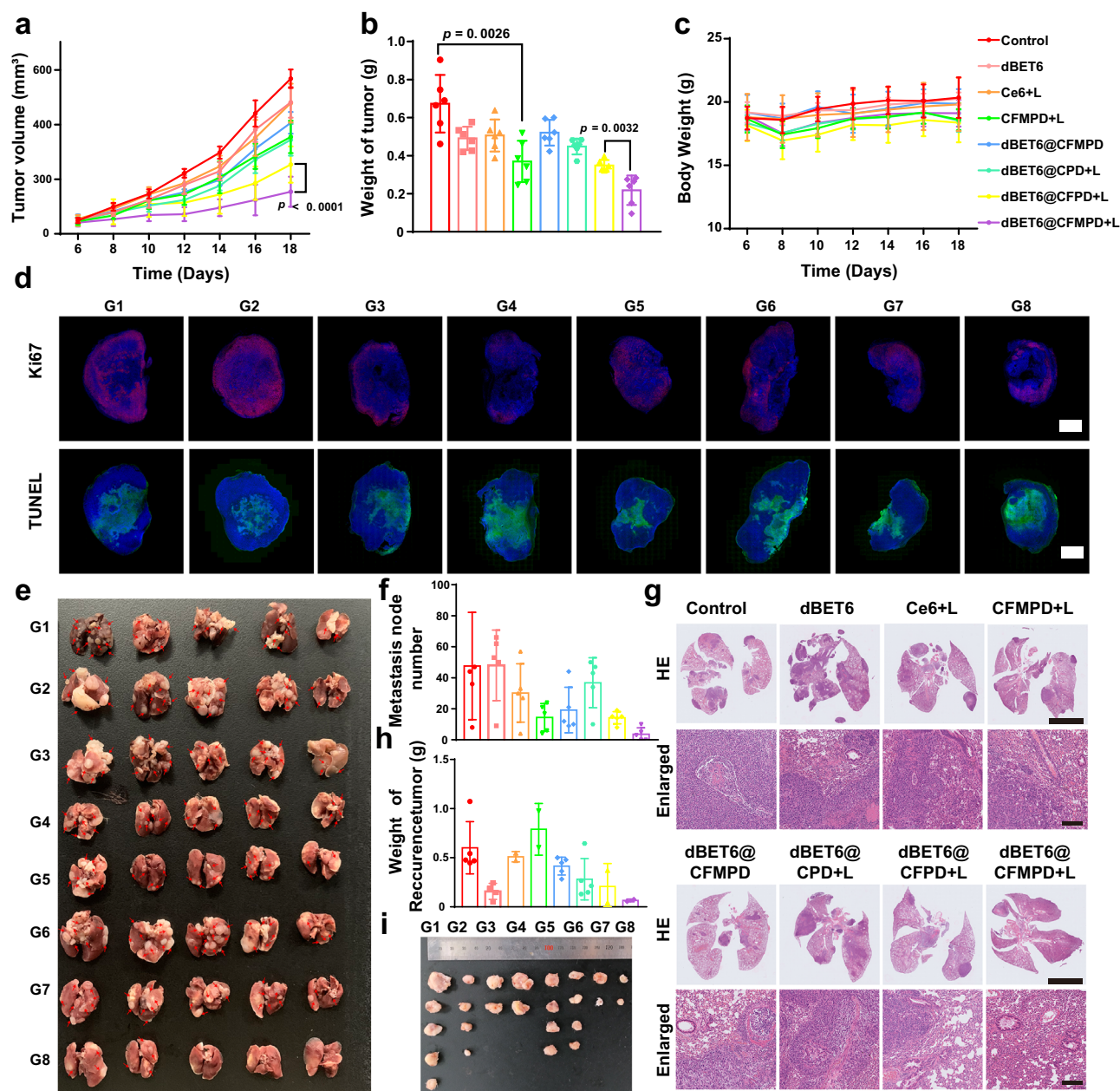


**Fig. 7 | In vivo antitumor and anti-metastasis effects.** **a** Tumor volume of 4T1 tumor-bearing mice recording every 2 days ( $n = 6$  mice). **b** Tumor weights of 4T1 breast cancer models ( $n = 6$  mice). **c** Body weight of mice administrated with different formulations ( $n = 6$  mice). **d** Ki67 and TUNEL staining assay of sectioned tumors (scale bar = 2 mm). **e**, **f** Ex vivo imaging and statistical results of lung metastases ( $n = 5$  mice). **g** HE staining images of lung tissues (scale bar = 5 mm in HE images, scale bar = 100  $\mu$ m in enlarged images). **h**, **i** Weights and ex vivo image of

recurrent tumors ( $n = 5$  mice). The G1–G8 represent Control, dBET6, Ce6+L, CFMPD+L, dBET6@CFMPD, dBET6@CPD+L, dBET6@CFPD+L, and dBET6@CFMPD+L, respectively. All data are presented as mean  $\pm$  SD. Two-tailed Student's  $t$  test and One-way analysis of variance (ANOVA) with a Tukey post hoc test were used for the statistical comparison between the two groups and among multiple groups, respectively. A significant difference was considered when the  $p$  value was  $< 0.05$ . Source data are provided as a Source Data file.

toxicity of all formulations (Supplementary Fig. 5a). Notably, there was mild inflammation in both control and treatment groups, including infiltration of inflammatory cells and blood cells, and thickening of the alveolar walls. However, there was no significant difference in lung H&E images between the control and nanoparticle groups, indicating that the lung inflammation was not induced by nanomedicines. Additionally, the blood samples were also collected to detect the biochemical parameters, including ALT (amino leucine transferase), AST (aspartate aminotransferase), ALP (alkaline phosphatase), CREA (creatinine), and LDH (lactate dehydrogenase). There were no significant changes in indicators of heart, kidney, and liver function (Supplementary Fig. 5b–f), suggesting the biosafety of nanomedicines. Meanwhile,

there were large necrotic areas in tumor sections for the dBET6@CFMPD+L group, according to the H&E images (Supplementary Fig. 5a). The ex vivo image of primary tumors also exhibited that dBET6@CFMPD+L induced strongest antitumor effect, comparing to other groups (Supplementary Fig. 6a). Moreover, TUNEL staining images were well consistent with the H&E analyses of tumor sections. PDT-containing groups exhibited strong TUNEL fluorescent signals, indicating the necrosis of tumor cells, which was improved by introducing BRD4 degradation and transformable shape (Fig. 7d). There were fewer Ki67 signals in PDT and combinational therapy groups, compared with the control group (Fig. 7d), suggesting less proliferation. These results indicated that the introduction of responsive shape

conversion and PROTAC could suppress tumor growth strongly, benefiting from specific distribution, enhanced retention, and combinational therapy.

After surgery removal of primary tumors, the lung metastasis models were constructed by intravenous injection of 4T1 cells. The lung tissues and recurrent tumors were collected and further analyzed. In Fig. 7e, there were more lung metastasis nodes in the Control and dBET6 groups. However, there were just a handful of metastasis nodes in the dBET6@CFMPD + L and dBET6@CFPD + L groups. dBET6@CFMPD + L treatment displayed the best anti-metastasis effect, followed by dBET6@CFPD + L and CFMPD + L (Fig. 7f). H&E staining results also showed the inhibition of dBET6@CFMPD + L on lung metastases, which were well consistent with the measurement of lung metastasis nodes (Fig. 7g). Meanwhile, the recurrent tumor weights were counted (Fig. 7h) and the ex vivo image of recurrent tumors was observed (Fig. 7i). These data showed that dBET6@CFMPD + L strongly

suppressed the development of recurrent tumors, whose number of and average weight of recurrent tumors were less than other groups. In a nutshell, these results jointly demonstrated that dBET6@CFMPD + L could not only suppress primary tumor growth but also inhibit the development of lung metastases and recurrence, which integrated enhanced retention by shape conversion, combinational therapy, and remodeling of immunosuppressive microenvironment.

### Inhibition of brain metastasis

Brain metastasis models were developed as previous methods with minor modifications to further investigate the anti-metastasis effect of nanomedicines. The brain metastasis growth was monitored by luminescence imaging after luciferase injection. On the 8th day post-injection of tumor cells, the mice were randomized to four groups according to the luminescence signals. Then the bioluminescence imaging was detected every 8 days. As shown in Fig. 8a, there were

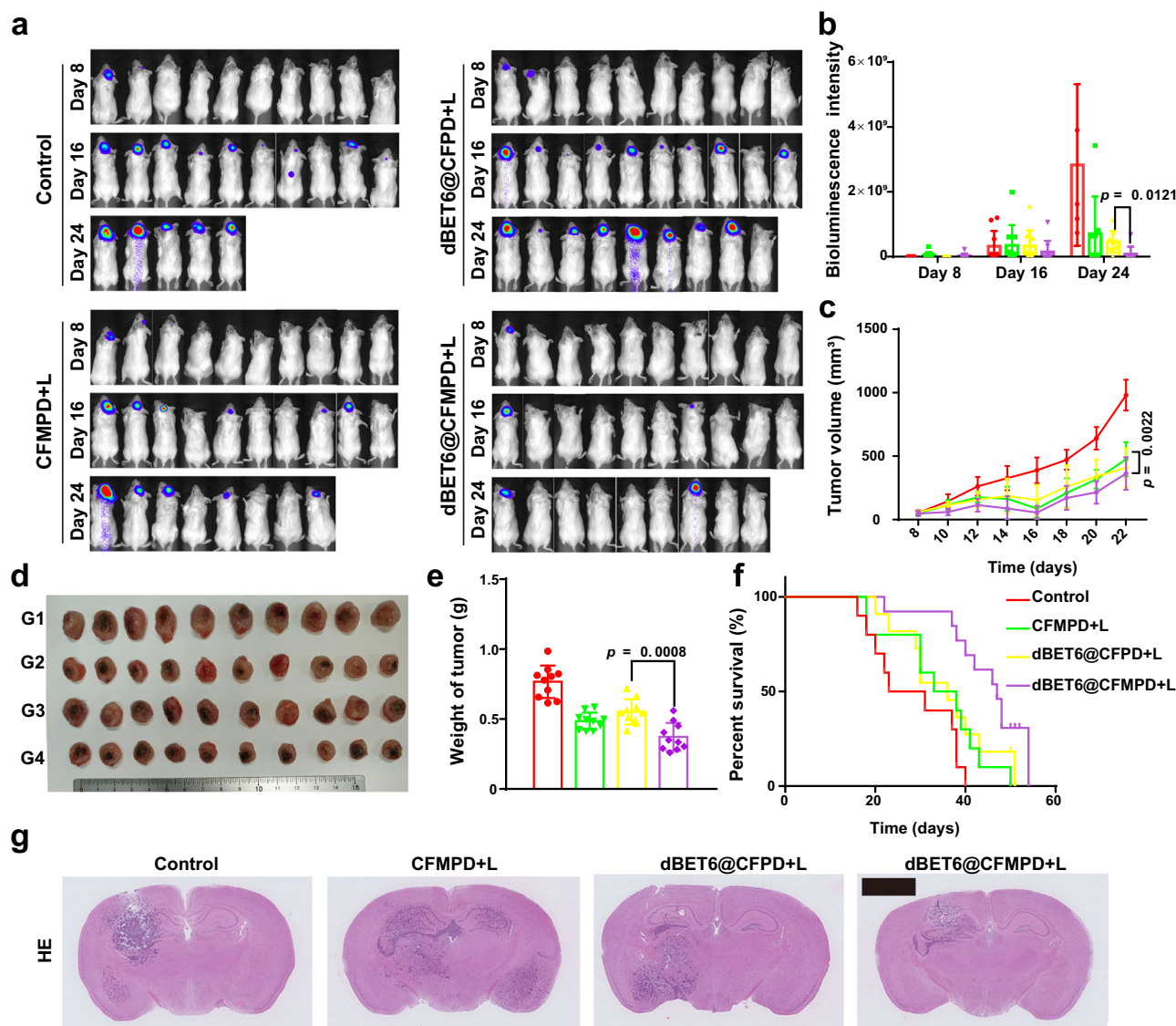


**Fig. 8 | Inhibition of primary and brain-metastatic tumors.** **a** Bioluminescence imaging of mice bearing with brain-metastatic tumors. **b** Semi-quantification results of bioluminescence imaging on the 8th, 16th, and 24th post-tumor inoculation ( $n = 10$  mice). **c** Tumor volume of primary tumors ( $n = 10$  mice). **d, e** The ex vivo image and weights of primary tumors ( $n = 10$  mice). The G1–G4 represent Control, CFMPD + L, dBET6@CFPD + L, and dBET6@CFMPD + L, respectively. **f** Percent survival analyses of mice bearing with brain-metastatic and primary

tumors ( $n = 10$  mice). And survival study was analyzed through Two-sided log-rank (Mantel–Cox) test. **g** H&E staining of brain tissues (scale bar = 2 mm). All data are presented as mean  $\pm$  SD. Two-tailed Student's  $t$  test and One-way analysis of variance (ANOVA) with a Tukey post hoc test were used for the statistical comparison between the two groups and among multiple groups, respectively. A significant difference was considered when the  $p$  value was  $< 0.05$ . Source data are provided as a Source Data file.



increased bioluminescence signals with time in the Control and dBET6@CFPD + L groups, and slightly increased signals with time in the CFMPD + L group. However, only several mice in the dBET6@CFMPD + L group displayed increased signals with time, indicating a considerable anti-metastasis effect. The semi-quantification results of bioluminescence imaging were similar to the monitor results (Fig. 8b). After the last treatment, the signal intensity of Control and dBET6@CFPD + L increased 780.0 times and 140.7 times compared to the signals on the 8th day, respectively. On the 24th day, dBET6@CFMPD + L-treated mice displayed the lowest bioluminescence signals, which were 5.71-fold and 8.84-fold lower than those in dBET6@CFPD + L and CFMPD + L groups, respectively. Meanwhile, the volume of the primary tumor was recorded every two days. The results were similar to the antitumor effect section (Fig. 8c). dBET6@CFMPD + L treatment showed the flattest growth curve, followed by dBET6@CFPD + L and CFMPD + L. On the 24th day, the primary tumors were removed by surgery to investigate the development and survival rate of brain metastases. The image of *ex vivo* tumors (Fig. 8d) and tumor weight (Fig. 8e) also demonstrated the antitumor effect of dBET6@CFMPD + L. Meanwhile, as the survival curve showed (Fig. 8f), dBET6@CFMPD + L treated mice exhibited longer median survival (47 days), which was 1.74-fold and 1.31-fold longer than mice in Control and dBET6@CFPD + L groups, respectively. As expected, there were fewer cancer cells in the brains of mice treated with dBET6@CFMPD + L than in other groups, according to the H&E staining (Fig. 8g). Therefore, the nanomedicine dBET6@CFMPD, which was equipped with transformable shape, mitochondria targeting, and combinational therapy, could inhibit the development of primary tumors and brain metastases.

### Immune response in vivo

To understand the anti-tumor and anti-metastasis mechanisms, the immune response in mice was explored after the last treatment of different formulations. Firstly, the ICD effect in vivo was observed. PDT induced potent CRT exposure and HMGB-1 secretion, which was further improved by the introduction of BRD4 inhibition and shape transformation (Fig. 9a). Then, the phenotype and abundance of immune cells in lymph nodes (LNs), spleens, and tumors were determined. There were more matured DCs (CD11c<sup>+</sup> CD80<sup>+</sup> CD86<sup>+</sup> cells) and T cells (CD3<sup>+</sup> CD4<sup>+</sup>/CD3<sup>+</sup> CD8<sup>+</sup> cells) in LNs and spleens from dBET6@CFMPD + L group than other groups, benefiting from increased antigen presentation and T cell activation induced by stronger ICD effect (Fig. 9b–e and Supplementary Fig. 6b–f). Additionally, the immune memory effect was investigated by flow cytometry. The percentages of central memory T cells (T<sub>cm</sub>, CD44<sup>+</sup> CD62L<sup>+</sup>) and effector memory T cells (T<sub>em</sub>, CD44<sup>+</sup> CD62L<sup>−</sup>) were detected, showing that the dBET6@CFMPD + L group induced the strongest local immunological memory and potential of long-term immunity to suppress tumor development and metastases, compared to other groups (Fig. 9f, g and Supplementary Fig. 6g).

T-cell activation and TAM repolarization in the tumor were also evaluated by flow cytometry. The percentages of IFN- $\gamma$ <sup>+</sup> CD8<sup>+</sup> T cells and CD4<sup>+</sup> T cells were both increased in the combinational therapy groups, suggesting enhanced T cell activation (Fig. 9h, i). Among them, the dBET6@CFMPD + L group showed a 2.32-fold higher percentage of IFN- $\gamma$ <sup>+</sup> CD8<sup>+</sup> T cells and a 2.27-fold higher percentage of CD4<sup>+</sup> T cells than the dBET6@CFPD + L group, due to shape transformation-improved retention and PDT efficiency. However, the abundance of T<sub>reg</sub> cells was increased in the CFMPD + L group (Fig. 9j). As reported, PDT induced the upregulation of PD-L1 while BRD4 degradation could decrease the expression of PD-L1 (Fig. 9k). dBET6@CFMPD + L showed 1.81-fold lower PD-L1 expression than CFMPD + L group. After the introduction of the BRD4 degradation, the number of T<sub>reg</sub> cells decreased and dBET6@CFMPD + L showed the lowest percentage of T<sub>reg</sub> cells. Meanwhile, the effect of various formulations on TAM

repolarization was studied using immunofluorescence staining and flow cytometry. The formulations containing BRD4 inhibitor could improve TAM repolarization from the M2 phenotype to the M1 phenotype, showing decreased CD206 and increased CD86 abundance (Fig. 9l, m). Moreover, the cytokines in the tumor were detected. dBET6@CFMPD + L group excreted high levels of cytokines for inhibiting tumor growth, such as TNF- $\alpha$ , and IFN- $\gamma$  (Supplementary Fig. 7a, b). Meanwhile, TGF- $\beta$ , and IL-10 suggesting immunosuppression and tumor survival, were significantly downregulated after the treatment (Supplementary Fig. 7c, d).

BRD4 degradation and EMT downregulation were investigated by WB analyses (Supplementary Fig. 7e). The dBET6-containing formulations induced strong degradation of BRD4 and c-Myc while an increase of E-cadherin and a reduction of Vimentin expression, indicating the downregulation of EMT. The results of immunofluorescence staining also showed the downregulation of EMT, and MMP-9, which would inhibit the invasion and migration of tumor cells, and also showed the decrease of PD-L1, and TAM repolarization (Supplementary Fig. 7f). All the above results signified that BRD4 inhibition-mediated PD-L1 downregulation and TAM repolarization in combination with shape conversion-enhanced retention and PDT via an MMP-2 sensitive nanomedicine provided an improved tumor immune response, which had great potential for the treatment of breast cancer and its lung metastases.

We then further investigated the immune response of primary and brain-metastatic tumor-bearing mice. Similarly, there were higher percentages of CD80<sup>+</sup> DCs and CD86<sup>+</sup> DCs in the LNs of dBET6@CFMPD + L treated mice than other formulation-treated mice. Meanwhile, in the LNs, the number of CD8<sup>+</sup> T cells and CD4<sup>+</sup> T cells were both increased in the combination therapy groups (Fig. 9n, o). The TAMs in brain metastatic tumors were also calculated by flow cytometry and immunofluorescence staining. There were upregulated M1 cells and reduced M2 phenotypes in the brains of mice treated with combination therapy (Fig. 9p, q). The results of immunofluorescence imaging also showed that there were the strongest CD206 signals (red fluorescence) and the weakest CD86 signals (green fluorescence) in the control group while reduced CD206 but increased CD86 signals in dBET6@CFMPD + L and dBET6@CFPD + L groups (Fig. 9r). These results verified the potential of dBET6@CFMPD for the treatment of brain metastases, by activation of immune response and TAM repolarization.

Briefly, these results jointly verified that the nanomedicines with MMP-triggered shape transformation and combination therapy of PDT and BRD4 inhibition could trigger potent ICD of tumor cells and remodel the immunosuppressive microenvironment, which induced DC maturation, T cell activation, and TAM repolarization to exert antitumor and anti-metastasis effects.

### Evaluation of anti-metastasis on E0771 models

The combination therapy efficiency of nanomedicines against breast cancer and brain metastasis was also investigated on E0771 models, using similar methods and techniques. The bioluminescence imaging of mice bearing brain-metastatic and primary tumors was detected every 8 days. There were heavily increased bioluminescence signals with time in the Control group, and slightly increased signals with time in the CFMPD + L and dBET6@CFPD + L groups (Fig. 10a). Only several mice in the dBET6@CFMPD + L group displayed increased signals with time, indicating a considerable anti-metastasis effect. The semi-quantification results of bioluminescence imaging were similar to the monitor results (Fig. 10b). Notably, dBET6@CFMPD + L treatment also exerted the strongest inhibitory effect against primary tumors, compared with other groups (Fig. 10c, d and Supplementary Fig. 8a). Meanwhile, the blood routine examination was carried out after treatment, including platelet count (PLT), red blood cell count (RBC), white blood cell count (WBC), mean platelet volume (MPV),



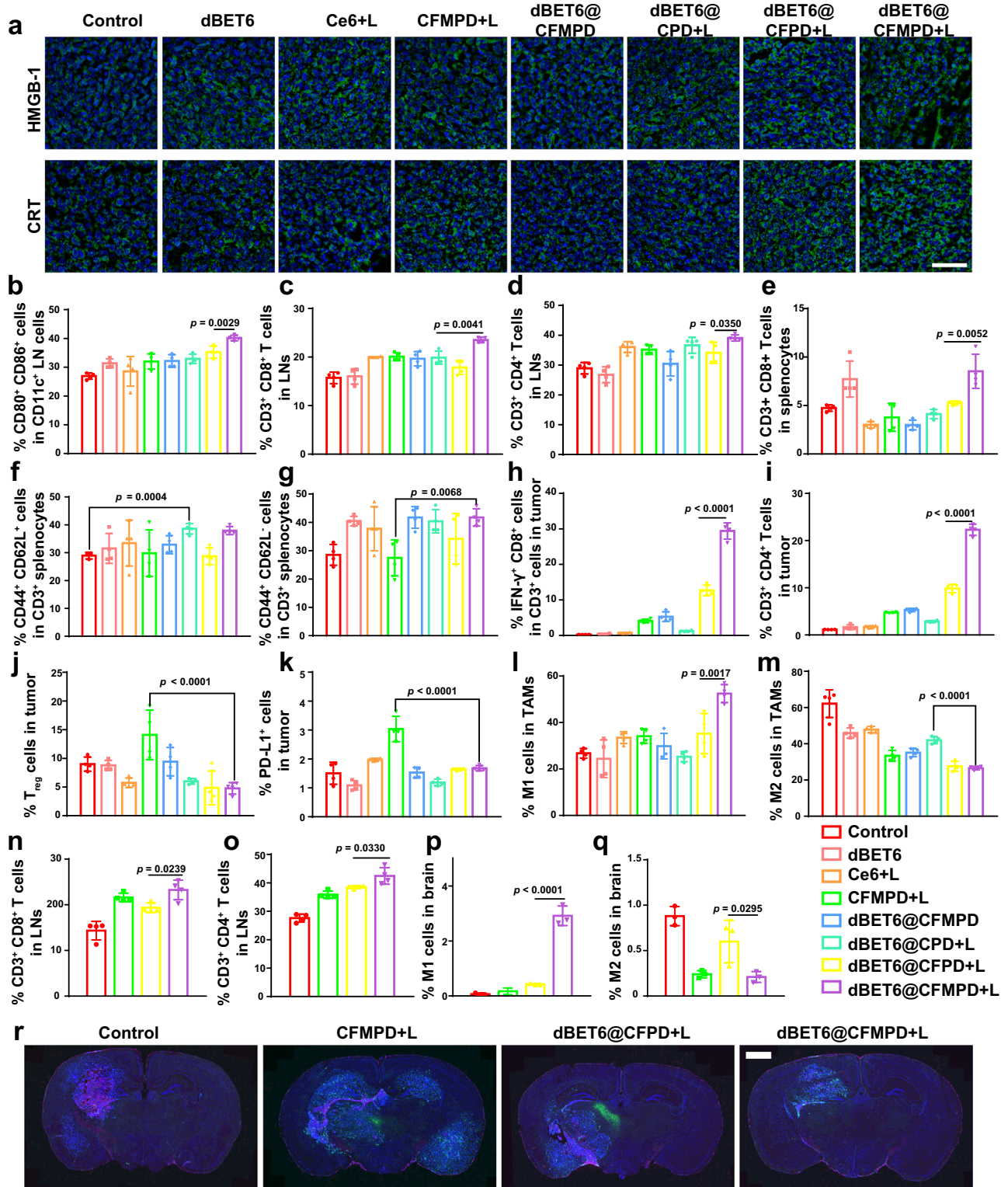


**Fig. 9 | In vivo antitumor immune response.** **a** Representative immunofluorescent images of tumor sections to detect the CRT and HMGB1 levels (scale bar = 50  $\mu$ m). **b–d** Percentages of CD80<sup>+</sup> CD86<sup>+</sup> DCs, CD8<sup>+</sup> T cells, and CD4<sup>+</sup> T cells in LNs. Quantification data of CD8<sup>+</sup> T cells (**e**), central memory T cells (Tcm, CD44<sup>+</sup>CD62L<sup>+</sup>) (**f**), and effector memory T cells (Tem, CD44<sup>+</sup>CD62L<sup>+</sup>) (**g**) in spleens. Abundances of IFN- $\gamma$ <sup>+</sup> CD8<sup>+</sup> T cells (**h**), CD4<sup>+</sup> T cells (**i**), and T<sub>reg</sub> cells (**j**) in tumors. **k** Percentages of PD-L1<sup>+</sup> cells in tumors after different treatments. Flow cytometry analyses of M1 (**l**) and M2 (**m**) cells in tumors. Flow cytometry measurements of CD8<sup>+</sup> T cells (**n**) and CD4<sup>+</sup> T cells (**o**) in the DLNs of mice bearing with primary and

brain metastatic tumors. Percentages of M1 (**p**) and M2 (**q**) cells in the brains after different treatments. **r** Representative immunofluorescent images of the brain to observe CD86<sup>+</sup> and CD206<sup>+</sup> cells (scale bar = 1 mm). Green and red fluorescence signals indicate CD86 and CD206, respectively.  $n = 4$  mice per group for all the studies. All data are presented as mean  $\pm$  SD. Two-tailed Student's  $t$  test and One-way analysis of variance (ANOVA) with a Tukey post hoc test were used for the statistical comparison between the two groups and among multiple groups, respectively. A significant difference was considered when the  $p$  value was  $< 0.05$ . Source data are provided as a Source Data file.

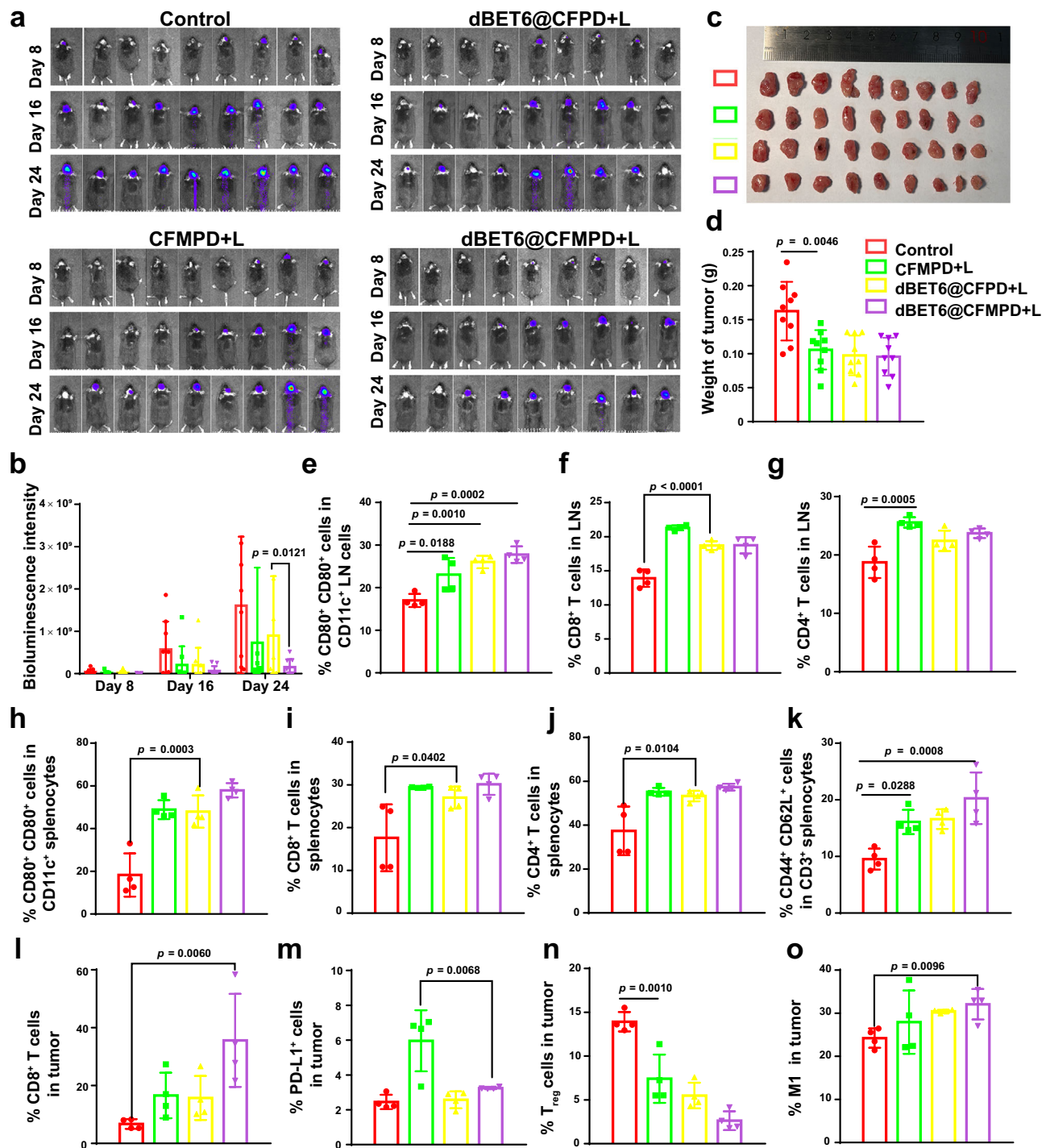


**Fig. 10 | Anti-metastasis effect and antitumor immune response on E0771-bearing mice.** **a** Bioluminescence imaging of mice bearing with brain-metastatic tumors. **b** Semi-quantification results of bioluminescence imaging on the 8th, 16th, and 24th post-tumor inoculation. **c, d** The ex vivo image and weights of primary tumors. **e–g** Percentages of CD80<sup>+</sup> CD86<sup>+</sup> DCs, CD8<sup>+</sup> T cells, and CD4<sup>+</sup> T cells in LNs. **h–k** Abundances of CD80<sup>+</sup> CD86<sup>+</sup> DCs, CD8<sup>+</sup> T cells, CD4<sup>+</sup> T cells, and Tcm cells in spleens. **l–o** Abundances of CD8<sup>+</sup> T cells, PD-L1<sup>+</sup> cells, T<sub>reg</sub> cells, and M1 cells in

tumors.  $n = 9$  mice per group for primary tumor growth and bioluminescence imaging studies in (**a, b, d**).  $n = 5$  mice per group for other studies. All data are presented as mean  $\pm$  SD. Two-tailed Student's *t* test and One-way analysis of variance (ANOVA) with a Tukey post hoc test were used for the statistical comparison between the two groups and among multiple groups, respectively. A significant difference was considered when the *p* value was  $< 0.05$ . Source data are provided as a Source Data file.

hemoglobin concentration (HGB), lymphocyte percentage (Lym%), and hematocrit (HCT). There was no obvious difference between the control and other groups, which indicated that dBET6 in nanomedicines did not induce thrombocytopenia, suggesting the biosafety of nanomedicines (Supplementary Fig. 8b–h). The antitumor immunity was also detected by flow cytometry. Similarly, there were strong DC

maturation and T-cell activation in the LNs and spleens of dBET6@CFMPD+L group, according to the percentages of CD80<sup>+</sup> CD86<sup>+</sup> DCs, CD8<sup>+</sup> T cells, and CD4<sup>+</sup> T cells (Fig. 10e–j). Interestingly, there were the highest ratios of Tcm cells in the mice treated with dBET6@CFMPD+L group, indicating strongest local immunological memory (Fig. 10k). The results of T cell infiltration in tumor also

showed potent antitumor response after treatment with PDT-PROTAC combination therapy (Fig. 10k and Supplementary Fig. 8i). The ratios of PD-L1<sup>+</sup> cells, T<sub>reg</sub> cells, and M2 cells in the tumor were heavily downregulated while the percentage of M1 cells increased after combination therapy, demonstrating the relief of immunosuppression (Fig. 10l–o and Supplementary Fig. 8j). These results verified the great potential of dBET6@CFMPD for the treatment of multiple models of breast cancer and brain metastasis, by integrating PDT-PROTAC nano-therapy and remodeling TIME.

## Discussion

PROTACs have the potential to treat refractory cancers because of their ability to effectively degrade tumor proteins. However, the clinical application of PROTACs is hampered by insufficient tumor-specific delivery and systemic adverse effects. Delivery of PROTAC drugs via nanotechnology is a viable strategy to improve the efficacy of PROTAC and reduce toxic side effects. The highly complex tumor micro-environment, such as dense stroma, higher solid stress, and high tissue fluid pressure, impedes the penetration and retention of nanomedicines within the tumor. Meanwhile, tumor sites exhibit unique properties such as weak acidity, highly expressed enzymes, highly expressed receptors, high levels of ROS, excess levels of GSH, and hypoxia, which have been utilized to construct responsive carriers to achieve efficient drug delivery and controlled release. To this end, we constructed a multifunctional nanomedicine dBET6@CFMPD to improve the tumor-specific accumulation of PROTAC and combine PROTAC with PDT, based on the MMP-2 responsive peptide sequence, which self-assembled into spherical nanoparticles with transformable shape and mitochondria targeting capacity, integrating improved penetration and retention.

After distribution and accumulation in the tumor, dBET6@CFMPD responded to MMP-2 and transformed into nanofibers, enhancing the retention of Ce6 to improve PDT efficiency and induce potent ICD. Meanwhile, the nanofibers accumulated in the mitochondria of tumor cells to induce mitochondria damage, due to targeting peptide sequence. On the other hand, dBET6 suppressed the expression of c-Myc and PD-L1 of tumor cells, inducing cell apoptosis via PROTAC. Moreover, dBET6 could repolarize TAMs to M1 phenotypes, synergizing with ICD and PD-L1 downregulation to remodel TIME and trigger strong antitumor immunity. Our data signify that multifunctional nanomedicine with a simple composition can integrate PROTAC and PDT-immunotherapy to reshape TIME and induce a potent antitumor immune response, thereby suppressing the development of primary and metastatic tumors and providing a strategy for cancer combination therapy.

## Methods

### Ethical statement

All animal experiments were performed under the guidelines, evaluated, and approved by the ethics committee of Sichuan University (No. K2022011).

### Cell lines

Murine 4T1 breast cancer cells, and 4T1-Luc cells were obtained from the Chinese Academy of Sciences Cells Bank (Shanghai, China). Murine E0771 breast cancer cells and E0771-Luc cells were purchased from IMMOCELL (Xiamen, Fujian, China). RAW264.7 cells were obtained from Haixing Biosciences (Suzhou, Jiangsu, China). These cell lines were authenticated using STR analysis and the last authenticated time of 4T1 is 10/05/2024, the E0771 is 29/04/2024, the RAW264.7 is 19/06/2024. All cell lines were tested negative for mycoplasma contamination. Complete RPMI-1640 or DMEM cell culture medium (containing 10% fetal bovine serum, 100 U/mL of penicillin G, and 100 U/mL of streptomycin sulfate) was prepared to culture cells. The complete culture medium for RAW264.7 cells was purchased from Haixing

Biosciences. The complete culture medium for E0771 and E0771-Luc breast cancer cells were purchased from IMMOCELL (Xiamen, Fujian, China).

### Animals

Female BALB/c mice (5–6 weeks, 18–22 g), female C57BL/6 mice (5–6 weeks, 18–22 g), and female BALB/c nude mice (5–6 weeks, 18–22 g) were purchased from SiPeiFu Biotechnology Co., Ltd. (Beijing, China). The animals were housed under SPF condition in groups of 10 mice per cage, and maintained at a temperature of -25 °C in a humidity-controlled environment with a 12 h light/dark cycle, and with free access to standard food and water. All experimental procedures involving animals were conducted in strict adherence to the guidelines of Institutional Animal Care and Use Committee (IACUC) of Sichuan University (No. K2022011). Female mice were chosen because the majority of metastatic breast cancers is seen in female patients. The maximal tumor size was not exceeded 1500 mm<sup>3</sup> during the experimental process.

### Materials

Chlorin e6 was purchased from J&K Scientific Ltd. (Beijing, China). MMP-2 responsive peptide (FFRKGPLGLAGC) and control peptide (FFRKGPGLLAGC) were attained from the Top peptide Company (Shanghai, China). BRD4 inhibitor dBET6 was purchased from Bide Pharmatech (Shanghai, China). DSPE-PEG<sub>2000</sub>-Mal and DSPE-PEG<sub>3400</sub>-NH<sub>2</sub> were purchased from Ponsure Biotechnology (Shanghai, China). Morpholin-4-yl-acetic acid hydrochloride, 1-(3-dimethylaminopropyl)-3 ethylcarbodiimide hydrochloride (EDC), 4-dimethylaminopyridine (DMAP) and trimethylamine (TEA) were purchased from Aladdin (Shanghai, China). 3-(4,5-dimethylthiazol-2-yl)-2,5-diphenyltetrazolium bromide (MTT) assay kit and collagenase IV were purchased from Biofrox (Einhausen, Germany). The annexin V-fluorescein isothiocyanate apoptosis detection kit and calcein-AM/PI assay kit were obtained from Yeasen (Shanghai, China). DCFH-DA and D-Luciferin were obtained from Meilunbio (Dalian, China). Anti-BRD4 (67374-2-Ig, 1:5000), anti-c-Myc (67447-1-Ig, 1:5000), anti-CD206 (18704-1-AP, 1:200), and anti-CD86 (13395-1-AP, 1:200) primary antibodies were purchased from Proteintech (Wuhan, China). Anti-CRT (ab92516, clone: EPR3924, 1:200), anti-HMGB-1 (ab18256, 1:1000), and Anti-CD31 (ab182981, clone: EPR17259, 1:2000) were purchased from Abcam. Anti-E-Cadherin (A22850, clone: ARC57093, 1:750), anti-Vimentin (A19607, clone: ARC0086, 1:2000), and anti-MMP-9 (A26079, clone: ARC68604, 1:200), anti-GAPDH (A19056, clone: ARC50888, 1:50000) primary antibodies were purchased from ABclonal (Wuhan, China). The anti-CD3-APC/Cy7 (100222, clone: 17A2, 1:300), anti-CD4-FITC (100406, clone: GK1.5, 1:500), anti-CD8-PE/Cy7 (100722, clone: 53-6.7, 1:300), anti-Foxp3-PE (126404, clone: MF-14, 1:300), anti-IFN-γ-APC (S05809, clone: XMGL2, 1:300), anti-CD11b-PE/Cy7 (101216, clone: M1/70, 1:300), anti-F4/80-FITC (123108, clone: BM8, 1:500), anti-CD86-PE (159204, clone: A17199A, 1:300), anti-CD206-APC (141708, clone: C068C2, 1:300), anti-PD-L1-APC (153616, clone: MIH6, 1:300), anti-CD11c-FITC (117306, clone: N418, 1:500), anti-CD80-PE/Cy7 (104734, clone: 16-10A1, 1:300), anti-CD86-APC (159216, clone: A17199A, 1:300), anti-CD44-FITC (103006, clone: IM7, 1:300), anti-CD62L-PE (104408, clone: MEL-14, 1:300) antibodies were purchased from BioLegend (San Diego, USA).

### Synthesis of Ce6-conjugated and PEGylated MMP-2 responsive peptide

Firstly, DSPE-PEG<sub>2000</sub>-modified transformable peptides (FFRKGPLGL AGC-PEG-DSPE) containing MMP-2-sensitive peptides were obtained by the addition reaction between the terminal sulphydryl group of the peptide and maleimide of DSPE-PEG-Mal. DSPE-PEG<sub>2000</sub>-Mal (0.1 mmol) and FFRKGPLGLGC-SH (0.11 mmol) were dissolved in 2 mL of N, N -Dimethylformamide (DMF), then triethylamine (TEA,



0.22 mmol) was added to adjust the pH value. This reaction was magnetically stirred overnight at 30 °C under nitrogen protection. Meanwhile, Ce6 (0.11 mmol), EDC (0.22 mmol), and NHS (0.22 mmol) were dissolved in 2 mL DMF, followed by the addition of TEA (0.24 mmol), and the mixture solution was stirred for 2 h to activate the carboxyl of Ce6. Finally, activated Ce6 was mixed with the reaction solution. After another 24 h reaction at 30 °C under nitrogen protection, Ce6-conjugated and PEGylated MMP-2 responsive peptide (CFMPD) was attained by dialysis (MWCO 2000) with 10% DMF overnight and with ultrapure water for 24 h, and lyophilization for 24 h. Ce6-conjugated and PEGylated control peptide (Ce6-FFRFKGPGLLAGC-PEG-DSPE, CFPD) was synthesized with similar methods, substituting control transformable peptide for MMP-2 responsive peptide. Ce6-PEG<sub>3400</sub>-DSPE (CPD) was obtained through an amide reaction between Ce6 and DSPE-PEG<sub>3400</sub>-NH<sub>2</sub>. The products were characterized by matrix-assisted laser desorption/ionization-time-of-flight mass spectrum (MALDI-TOF-MS, Shimadzu, Japan).

### Preparation and characterization of nanoparticles

According to previous work, the preparation method was as follows with minor modifications. CFMPD (CFPD/CPD) and dBET6 were dissolved in DMF, respectively. Then the two were ultrasonically mixed at a ratio of CFMPD (CFPD/CPD): BET6 = 10:1 and subsequently dropped into 15 times the volume of ultrapure water with stirring. After stirring for 5 min, the mixture was subsequently ultrasonized using an ultrasonic cell crusher (65 W, 5 s/5 s a cycle for 5 min). The DMF was removed and nanomedicines (dBET6@CFMPD/ dBET6@CFPD, dBET6@CPD) were concentrated by centrifugal filters (MWCO 10 kDa, Millipore). The sizes and zeta-positions of nanomedicines were monitored by dynamic light scattering (DLS, Brookhaven). The morphology and particle size of these nanoparticles were observed by transmission electronic microscopy (TEM, H-600, Hitachi, Japan). Similarly, CFMPD/CFPD/CPD were prepared and characterized using the same method.

### MMP-2 responsive capacity

To test the MMP-2 responsiveness, Ce6-FFRFKGPGLLAGC-PEG-DSPE (CFMPD), and Ce6-FFRFKGGLLAGC-PEG-DSPE (CFPD) were cultured with human MMP-2 enzyme for 4 h or 24 h at 37 °C, respectively. MALDI-TOF-MS monitored the molecular weight changes. Moreover, the size and morphology changes of dBET6@CFMPD/ dBET6@CFPD were monitored by DLS and measured by TEM, after being treated with the MMP-2 enzyme.

### Cellular uptake

4T1 cells were planted into 12-well plates at a density of  $1 \times 10^5$  per well and grew to 80% confluency. Free Ce6, CPD, CFPD, and CFMPD were dispersed in serum-free 1640 medium and added to the wells at the same concentration of Ce6 (5 µg/mL). After being treated with different formulations for 1, 4, and 12 h, the cells were collected and measured by flow cytometry (Agilent, NovoCyt). Meanwhile, 4T1 cells ( $2 \times 10^5$  per well) were seeded onto a 12-well plate preplaced with coverslip and cultured for 36 h to grow until 60% confluency. The cells were treated as described above, washed with cold PBS, fixed, and stained with DAPI (1 µg/ml) for 5 min. For the qualitative assay, the fluorescence intensity was imaged by fluorescent microscope (Leica, Germany). To investigate the effect of shape transformation on cellular uptake, CPD, CFPD, and CFMPD were pretreated with MMP-2 for 12 h and incubated with 4T1 cells for 1, 2, and 4 h. The fluorescence intensity was measured and monitored by flow cytometry and CLSM.

### In vitro retention

Eighty µL of 2% low melting point agarose (dissolved in serum-free DMEM medium) was added to a 96-well plate, allowing it to gelatinize. A total of  $5 \times 10^3$  4T1 cells were seeded on the pre-gelatinized wells.

Four days later, the uniform multicellular spheroids (MSCs) were cultured with CPD, CFPD, and CFMPD at an equivalent concentration of Ce6 (5 µg/mL). 12 h later, the nanomedicine-containing medium was removed and replaced with the fresh culture medium. After incubation for another 12 h, the MSCs were collected, washed, and fixed. Confocal laser scanning microscope (CLSM) observed the fluorescence of Ce6 to investigate the retention of shape-transformable nanomedicines.

### Intracellular localization

Well-grown 4T1 cells were inoculated at a density of  $1 \times 10^5$  cells per well in a cell culture dish with a circular slide (15 mm in diameter) at the bottom and incubated at 37 °C to grow 80% confluency. The cells were treated with different formulations for 4 h. Then, the Mito-Tracker Red was diluted to 50 nM with serum-free medium, added to the dishes, and placed in the incubator for 30 min for staining. After being washed with cold PBS, the cells were observed by fluorescent microscope to evaluate the colocalization of nanoparticles with mitochondria.

### ROS generation in vitro

4T1 cells were planted in 12-well plates at a density of  $1 \times 10^5$  per well and allowed to grow to 80%. The cells were incubated with various dispersions for 12 h. The medium formulation was removed and replaced with DCFH-DA (10 µM). The laser irradiation was given. After being cultured for another 2 h, the cells were washed with cold PBS and collected to detect the fluorescence signals of DCF in different groups.

### Anti-tumor effect in vitro

Cytotoxicity of different formulations on 4T1 cells or RAW264.7 cells was explored by MTT assay.  $5 \times 10^3$  per well of 4T1 or RAW 264.7 cells were planted into 96-well plates and grew for 24 h. The cells were incubated with various preparations with different concentrations. 4 h later, the laser irradiation groups were irradiated by 650 nm laser, and incubated for another 20 h. The cytotoxicity was evaluated by MTT assay.

Anti-tumor effect in vitro was also carried out by live/dead staining assay. 4T1 cells were seeded in 96-well plates, followed by different treatments for 4 h. Then, the laser irradiation was conducted. Post another 4 h incubation, the cells were stained with Calcein-AM (5 µg/mL) and PI (10 µg/mL), and imaged by fluorescent microscope.

Apoptosis assay was also evaluated on 4T1 cells. 4T1 cells were cultured in 12-well plates as described above. Following different treatments as mentioned as live/dead staining assay, the cells were collected to stain with Annexin V-FITC and PI before flow cytometry detection.

### Inhibition of BRD4 and c-Myc

For western blot (WB) analyses of BRD4 inhibition, 4T1 cells were planted into 6-well plates at a density of  $2 \times 10^5$  per well. After growing to 60% confluency, the cells were treated with different concentrations of free dBET6 for 24 h. The cells were washed with cold PBS, and incubated with RIPA buffer over ice supplement with protease inhibitors (PMSF). The cell lysates were collected. After centrifugation, the protein concentrations of different groups were detected by the BCA assay kit, and the protein samples were mixed with loading buffer and denatured by heating at 100 °C for 10 min. Protein samples were separated by molecular weight size by polyacrylamide gel electrophoresis. The expression levels of BRD4 and c-Myc were monitored by WB analysis. Moreover, the suppression effects on BRD4 and c-Myc of dBET6-based nanomedicines were also investigated by WB analysis, including Ce6@dBET6, CFMPD, dBET6@CPD, dBET6@CFPD, dBET6@CFMPD.

### PD-L1 downregulation in vitro

PD-L1 blockade on 4T1 cells was detected by flow cytometry. Briefly, 4T1 cells were treated with 100 ng/mL of IFN-γ to upregulate PD-L1

expression. Then the cells were treated with dBET6, Ce6&dBET6+L, CFMPD + L, dBET6@CPD + L, dBET6@CFPD + L, dBET6@CFMPD, and dBET6@CFMPD + L were given the same Ce6 and BET6 concentrations to cells (0.5 µg/mL of Ce6, 0.25 µg/mL of dBET6). The cells received laser irradiation after incubation for 4 h. 24 h later, the cells were collected and stained by PD-L1 antibody, finally detected by flow cytometry and CLSM.

### In vitro ICD response assessment

4T1 cells were seeded in 12-well plates and cultured for 24 h to 80% confluency. The fresh medium or medium containing different formulations (dBET6, Ce6 + L, dBET6&Ce6 + L, CFMPD + L, dBET6@CPD + L, dBET6@CFPD + L, dBET6@CFMPD, dBET6@CFMPD + L) were introduced into wells. Post 4 h incubation, laser exposure was carried out. 2 h later, the culture supernatants were collected to detect the released HMGB-1 (HMGB-1 ELISA kit, Ruixin Biotech) and ATP (ATP Assay kit, Beyotime). The cells were collected, washed with cold PBS, and stained with anti-CRT primary antibody for 1 h. Followed by FITC-labeled secondary antibody, the exposure levels of CRT on the cell surface were measured by flow cytometry. Meanwhile, the qualitative results of CRT translocation were obtained by immunofluorescence analysis. 4T1 cells were treated as mentioned above, then the cells were fixed and stained with anti-CRT antibody at 4 °C overnight. Finally, the cells were stained with FITC-labeled secondary antibody and DAPI before detection by fluorescent microscope.

### In vitro macrophage repolarization

RAW264.7 cells ( $1 \times 10^5$  cells per well) were planted in 12-well plates and cultured for 12 h to allow adhesion. To obtain M2-type macrophages, the cells were incubated with IL-4 (20 ng/mL) for 12 h. Then, the M2-type macrophages were treated with different formulations at equivalent contents of dBET6 (0.25 µg/mL). Post 4 h incubation, laser irradiation was conducted. After 24 h, the supernatants were collected to measure the inflammatory and anti-inflammatory cytokine levels. The cells were washed, collected, and stained with APC/Cy7-CD86 and FITC-CD206 to evaluate the M1- or M2-like macrophage ratio by flow cytometry.

### Wound healing

As mentioned, 4T1 cells were cultured in 12-well plates and grew to 80% confluency. The cell monolayers were scraped with a 10 µL tip and washed thrice with cold PBS to remove suspended cells. Different treatments were conducted, including Ce6, dBET6&Ce6, CPD, CFMPD, dBET6@CPD, dBET6@CFPD, dBET6@CFMPD. Post 4 h incubation, laser exposure was carried out. After 24 h, the cells were fixed and stained 0.1% crystal violet (Solarbio). The migration of cells into the scratched area was observed using an inverted microscope (Olympus). The wound healing rate was calculated: cell motility (%) = 1 - wound area at 24 h/wound area at 0 h.

### In vitro anti-metastasis effect

Migration and invasion assays were conducted as reported previously. Briefly, the transwell plates (Corning 3422) were placed in the incubator overnight to get equilibrium, where top chambers were added with serum-free medium. In contrast, the bottom chambers were filled with serum-containing medium. For migration assay,  $2 \times 10^5$  4T1 cells were added to the top chambers and treated with different formulations. Post 4 h incubation, the laser groups received laser irradiation. After 24 h treatment, the migrated cells were fixed, stained with 0.1% crystal violet, and imaged by microscope. Next, the crystal violet was eluted with 33% acetic acid solution, and the absorbance was detected at 570 nm. For invasion assay, the Matrigel Matrix (BD Biosciences) was added to top chambers before 4T1 cell plantation. The subsequent operations were consistent with the migration assay.

### Biodistribution and retention in vivo

BALB/c nude mice bearing primary tumors of breast cancer were constructed as the previous method. After -14 days of injection, mice bearing tumors around 200 mm<sup>3</sup> were randomly divided into four groups ( $n = 4$  mice), including Ce6, CPD, CFPD, and CFMPD. Post intravenous injection, the fluorescence images of biodistribution analyses were obtained by IVIS Lumina imaging system (PerkinElmer, USA) at 1, 2, 4, 8, 12, and 24 h. After administration for 24 h, the mice were sacrificed, and the tumors and major organs were collected to attain ex vivo fluorescence images. The tumors and major organs were fixed, dehydrated, and frozenly sectioned for fluorescent imaging.

To investigate the retention effect of shape-transformable nanomedicines, CFPD and CFMPD were intratumorally administrated to BALB/c nude mice bearing breast cancer. The in vivo fluorescence images were observed using the IVIS Lumina imaging system at 5 min, 4, 8, 12, 24, 36, and 48 h post-injection. The ex vivo fluorescence and section images were also detected as mentioned above.

### Evaluation of BBB penetration and brain accumulation

The bEnd.3 cells were inoculated into the upper chamber (Corning 3415, 24 well, 3 µm, USA) and cultured until the transendothelial resistance peaked and stabilized. Subsequently, the bottom chamber was seeded with 4T1. Serum-free DMEM medium containing Ce6, CPD, CFPD, and CFMPD was added to the upper chamber when 4T1 cells had grown to 80% confluency. The BBB penetration efficiencies of preparations were evaluated by measuring the nanoparticle fluorescence in the lower chamber supernatant and the uptake of nanoparticles by 4T1 cells. 3D confocal imaging was observed to evaluate the penetration of nanomedicines in the bEnd.3 monolayer.

Brian-metastasis model of breast cancer was developed by intracranially implanting the 4T1-Luc cells ( $5 \times 10^3$ ) into the right hippocampus using a stereotaxic apparatus. After 10 days of injection, the mice were divided into four groups ( $n = 4$  mice) according to the bioluminescence intensity, including Ce6, CPD, CFPD, and CFMPD groups. Post intravenous injection, the fluorescence images of biodistribution analyses were obtained by the IVIS Lumina imaging system at 1, 2, 4, and 8 h to investigate the targeting distribution and accumulation of nanomedicines in the brain. At 8 h post-injection, the mice were sacrificed, and the brains and major organs were collected to obtain ex vivo fluorescence images.

### Anti-tumor and anti-lung metastasis in vivo

4T1 cells ( $2 \times 10^5$ ) were subcutaneously injected into the third left mammary fat pad of BALB/c mice to construct breast cancer models. Mice-bearing tumors around 80 mm<sup>3</sup> were randomized into 8 groups ( $n = 6$  mice). The mice were treated with 5% glucose (as control), dBET6, Ce6 + L, CFMPD + L, dBET6@CFMPD, dBET6@CPD + L, dBET6@CFPD + L, dBET6@CFMPD + L every five days, respectively, at the same dosages of Ce6 (2.5 mg/kg) and dBET6 (1.25 mg/kg). The laser irradiation was conducted at 4 h and 24 h post-injection. The volume of tumors and body weight were recorded every 2 days. The same treatment experiments were performed on additional mice to collect serum and organs to determine systemic side effects and tumor cell apoptosis. On the day after the last dose, 4 mice per group were randomly executed and serum, tumor, and major organs were collected for biochemical parameters, immune response assessment, and HE staining. Post 18 days injection of tumor cells, the primary tumors were excised, and 4T1 cells ( $2.5 \times 10^5$ ) were intravenously injected to construct lung metastasis models. Lungs and recurrent tumors from mice that died from recurrence and metastasis in the experiment were collected for counting and photographing purposes. 16 days later, the remaining mice were sacrificed to calculate metastasis nodes. The number of metastasis nodes was calculated as  $I \times 1 + II \times 2 + III \times 3 + IV \times 4 + V \times 5 + VI \times 10$  (grade I < 0.5 mm; 0.5 mm ≤ grade II < 1 mm; 1 mm ≤ grade III < 2 mm; 2 mm ≤



grade IV < 3, 3 mm ≤ grade IV < 5, VI > 5 mm). In addition, ex vivo lungs were made slices for H&E assay.

### In vivo anti-brain metastasis

Brain-metastasis model of breast cancer was developed by intracranially implanting the 4T1-Luc cells ( $2 \times 10^3$ ) or E0771-Luc cells ( $5 \times 10^3$ ) into the right hippocampus using a stereotaxic apparatus. Meanwhile, 4T1 cells ( $2 \times 10^5$ ) or E0771 cells ( $5 \times 10^5$ ) were subcutaneously injected into the third mammary fat pad to allow the development of primary tumors. 8 days later, the mice were intraperitoneally injected with D-luciferin potassium (150 mg/kg), and the bioluminescence images were obtained using the IVIS Lumina imaging system at 10–15 min post-injection. The mice were divided into 4 groups according to the bioluminescence intensity ( $n = 9$  or 10 mice), including Control, CFMPD + L, dBET6@CFPD + L, and dBET6@CFMPD + L. The dosing regimen was as described above. On the 16th and 24th-day post-tumor cell injection, the bioluminescence imaging was obtained using a similar method. The tumor volume and body weight were recorded every 2 days. The same therapy experiment was performed on several additional mice. The day after the last administration, 3 or 4 mice in every group were randomly selected and sacrificed to harvest brains, DLNs (cervical lymph nodes), and spleens. On the 24th day, the primary tumors were removed by surgery. The body weight was recorded every day. Mice with 10% weight loss, hemiplegia, blindness, and feeding difficulties were recorded as animal endpoints.

### Immune response assessment in vivo

To obtain single-cell suspensions of tumors, tissues were mechanically dissected and incubated with 30 U/mL DNase, 175 U/mL Collagenase IV, and 100 U/mL HAase for 1 h, then filtered through a 75  $\mu$ m filter. Similarly, DLNs were incubated with 175 U/mL collagenase for 1 h and then passed through a sieve to obtain lymph node single-cell suspensions. Splenic tissues were passed through a sieve mesh and then treated with erythrocyte lysate to finally obtain splenocyte single-cell suspension. The cells were collected and washed twice with PBS before staining to evaluate immune response.

Tumor tissues were collected and incubated in RIPA buffer containing 1 mM PMSF and ground with grinding beads. The ground samples were centrifuged (12,000 g, 10 min) and the supernatant was collected. The supernatant was analyzed for levels of TNF- $\alpha$ , IFN- $\gamma$ , IL-10, and TGF- $\beta$  using an ELISA kit according to the instructions.

### Statistical analysis and reproducibility

All data were presented as mean  $\pm$  SD. Statistical analysis was performed using GraphPad Prism software 7.00. Two-tailed Student's *t* test and One-way analysis of variance (ANOVA) with a Tukey post hoc test were used for the statistical comparison between the two groups and among multiple groups, respectively. And survival study was analyzed through Two-sided log-rank (Mantel–Cox) test. A significant difference was considered when the *p* value was less than 0.05. Dots overlaid on the bar graphs are the value measured for biological replicates. The micrographs are representative images ( $n = 3$  biological replicates). No statistical method was used to predetermine sample size. No data were excluded from the analyses. The experiments were randomized. The investigators were blinded to allocation during experiments and outcome assessment.

### Reporting summary

Further information on research design is available in the Nature Portfolio Reporting Summary linked to this article.

### Data availability

All data supporting the results of this study are available within the paper, Supplementary Information or Source data files. The mass

spectrometry data are available in the Supplementary Information. Source data are provided with this paper.

### References

- Burslem, G. M. & Crews, C. M. Proteolysis-targeting chimeras as therapeutics and tools for biological discovery. *Cell* **181**, 102–114 (2020).
- Li, K. & Crews, C. M. PROTACs: past, present and future. *Chem. Soc. Rev.* **51**, 5214–5236 (2022).
- Bauer, K. et al. Degradation of BRD4—a promising treatment approach not only for hematologic but also for solid cancer. *Am. J. Cancer Res.* **11**, 530–545 (2021).
- Wang, F. et al. Dual-programmable semiconducting polymer NanoPROTACs for deep-tissue sonodynamic-ferroptosis activatable immunotherapy. *Small* **20**, 2306378 (2023).
- Yang, C., Yang, Y., Li, Y., Ni, Q. & Li, J. Radiotherapy-triggered proteolysis targeting chimera prodrug activation in tumors. *J. Am. Chem. Soc.* **145**, 385–391 (2023).
- Cotton, A. D., Nguyen, D. P., Gramespacher, J. A., Seiple, I. B. & Wells, J. A. Development of antibody-based PROTACs for the degradation of the cell-surface immune checkpoint protein PD-L1. *J. Am. Chem. Soc.* **143**, 593–598 (2021).
- Liu, J. et al. Cancer selective target degradation by Folate-Caged PROTACs. *J. Am. Chem. Soc.* **143**, 7380–7387 (2021).
- He, S. et al. Aptamer-PROTAC conjugates (APCs) for tumor-specific targeting in breast cancer. *Angew. Chem. Int. Ed.* **60**, 23299–23305 (2021).
- Gao, J. et al. Engineered bioorthogonal POLY-PROTAC nanoparticles for tumour-specific protein degradation and precise cancer therapy. *Nat. Commun.* **13**, 4318 (2022).
- Zhou, Z., Song, J., Nie, L. & Chen, X. Reactive oxygen species generating systems meeting challenges of photodynamic cancer therapy. *Chem. Soc. Rev.* **45**, 6597–6626 (2016).
- Deng, K. et al. Recent progress in near infrared light triggered photodynamic therapy. *Small* **13**, 1702299 (2017).
- Ren, C. et al. Dual-action nanoplatform with a synergetic strategy to promote oxygen accumulation for enhanced photodynamic therapy against hypoxic tumors. *Acta Biomater.* **146**, 465–477 (2022).
- Kumar, A., Moralès, O., Mordon, S., Delhem, N. & Boleslawski, E. Could photodynamic therapy be a promising therapeutic modality in hepatocellular carcinoma patients? A critical review of experimental and clinical studies. *Cancers* **13**, 5176 (2021).
- Krysko, D. V. et al. Immunogenic cell death and DAMPs in cancer therapy. *Nat. Rev. Cancer* **12**, 860–875 (2012).
- Castano, A. P., Mroz, P. & Hamblin, M. R. Photodynamic therapy and anti-tumour immunity. *Nat. Rev. Cancer* **6**, 535–545 (2006).
- Ng, C. W., Li, J. & Pu, K. Recent progresses in phototherapy-synergized cancer immunotherapy. *Adv. Funct. Mater.* **28**, 1804688 (2018).
- Xiong, W. et al. Metformin liposome-mediated PD-L1 down-regulation for amplifying the photodynamic immunotherapy efficacy. *ACS Appl. Mater. Interfaces* **13**, 8026–8041 (2021).
- Zhang, X. et al. Inhibiting COX-2/PGE2 pathway with biodegradable NIR-II fluorescent polymeric nanoparticles for enhanced photodynamic immunotherapy. *Nano Today* **48**, 101759 (2023).
- Zheng, C. et al. Killing three birds with one stone: multi-stage metabolic regulation mediated by clinically usable berberine liposome to overcome photodynamic immunotherapy resistance. *Chem. Eng. J.* **454**, 140164 (2023).
- Jiang, X. et al. Role of the tumor microenvironment in PD-L1/PD-1-mediated tumor immune escape. *Mol. Cancer* **18**, 10 (2019).
- Keir, M. E., Butte, M. J., Freeman, G. J. & Sharpe, A. H. PD-1 and its ligands in tolerance and immunity. *Annu. Rev. Immunol.* **26**, 677–704 (2008).

22. Ovais, M., Guo, M. & Chen, C. Tailoring nanomaterials for targeting tumor-associated macrophages. *Adv. Mater.* **31**, 1808303 (2019).
23. Ngambenjawong, C., Gustafson, H. H. & Pun, S. H. Progress in tumor-associated macrophage (TAM)-targeted therapeutics. *Adv. Drug Deliv. Rev.* **114**, 206–221 (2017).
24. Yang, Q. et al. The role of tumor-associated macrophages (TAMs) in tumor progression and relevant advance in targeted therapy. *Acta Pharm. Sin. B* **10**, 2156–2170 (2020).
25. Jing, X. et al. BRD4 inhibition suppresses PD-L1 expression in triple-negative breast cancer. *Exp. Cell Res.* **392**, 112034 (2020).
26. Zhu, H. et al. BET bromodomain inhibition promotes anti-tumor immunity by suppressing PD-L1 expression. *Cell Rep.* **16**, 2829–2837 (2016).
27. Yang, T. et al. A BRD4 PROTAC nanodrug for glioma therapy via the intervention of tumor cells proliferation, apoptosis and M2 macrophages polarization. *Acta Pharm. Sin. B* **12**, 2658–2671 (2022).
28. Zhang, H.-T. et al. Versatile Nano-PROTAC-induced epigenetic reader degradation for efficient lung cancer therapy. *Adv. Sci.* **9**, 2202039 (2022).
29. Matthews, G. M. et al. BET bromodomain degradation as a therapeutic strategy in multiple myeloma. *Blood* **128**, 1062–1062 (2016).
30. Zhu, X. et al. The BET PROTAC inhibitor dBET6 protects against retinal degeneration and inhibits the cGAS-STING in response to light damage. *J. Neuroinflammation* **20**, 119 (2023).
31. Maeda, H. Toward a full understanding of the EPR effect in primary and metastatic tumors as well as issues related to its heterogeneity. *Adv. Drug Deliv. Rev.* **91**, 3–6 (2015).
32. Qin, Y. et al. Self-delivered supramolecular nanomedicine with transformable shape for ferrocene-amplified photodynamic therapy of breast cancer and bone metastases. *Adv. Funct. Mater.* **31**, 2104645 (2021).
33. Yu, W. et al. Sequentially responsive biomimetic nanoparticles with optimal size in combination with checkpoint blockade for cascade synergetic treatment of breast cancer and lung metastasis. *Bio-materials* **217**, 119309 (2019).
34. Liu, R. et al. Linear chimeric triblock molecules self-assembled micelles with controllably transformable property to enhance tumor retention for chemo-photodynamic therapy of breast cancer. *Adv. Funct. Mater.* **29**, 1808462 (2019).
35. Jia, W., Wang, Y., Liu, R., Yu, X. & Gao, H. Shape transformable strategies for drug delivery. *Adv. Funct. Mater.* **31**, 2009765 (2021).
36. Lin, C. et al. GSH-responsive SN38 dimer-loaded shape-transformable nanoparticles with iRGD for enhancing chemo-photodynamic therapy. *Acta Pharm. Sin. B* **10**, 2348–2361 (2020).
37. Habibi, N., Kamaly, N., Memic, A. & Shafiee, H. Self-assembled peptide-based nanostructures: smart nanomaterials toward targeted drug delivery. *Nano Today* **11**, 41–60 (2016).
38. Görbitz, C. H. The structure of nanotubes formed by diphenylalanine, the core recognition motif of Alzheimer's  $\beta$ -amyloid polypeptide. *Chem. Commun.* **22**, 2332–2334 (2006).
39. Wu, C. et al. Nanofibrillar peptide hydrogels for self-delivery of lonidamine and synergistic photodynamic therapy. *Acta Biomater.* **155**, 139–153 (2023).
40. Lei, E. K. & Kelley, S. O. Delivery and release of small-molecule probes in mitochondria using traceless linkers. *J. Am. Chem. Soc.* **139**, 9455–9458 (2017).
41. Donati, B., Lorenzini, E. & Ciarrocchi, A. BRD4 and cancer: going beyond transcriptional regulation. *Mol. Cancer* **17**, 164 (2018).
42. Liao, Y.-F. et al. High level of BRD4 promotes non-small cell lung cancer progression. *Oncotarget* **7**, 9491–9500 (2016).

## Acknowledgements

The work is supported by the National Natural Science Foundation of China (82173762 to H.G.), and the Fundamental of Research Funds for the Central Universities.

## Author contributions

Fan Tong and Huile Gao conceived the project and strategies. Fan Tong and Yufan Wang designed and carried out the experiments, analyzed data, and wrote the manuscript. Huile Gao, Yang Zhou, and Tao Gong supervised the work and corrected the manuscript. Yanyan Xu, Siqin He, Yufan Du, Wenqin Yang, Ting Lei, Yujun Song participated the experimental work on the therapeutic efficacy and corrected the manuscript. All authors read and approved the final manuscript.

## Competing interests

The authors declare no competing interests.

## Additional information

**Supplementary information** The online version contains supplementary material available at <https://doi.org/10.1038/s41467-024-54854-2>.

**Correspondence** and requests for materials should be addressed to Huile Gao.

**Peer review information** *Nature Communications* thanks Jacques Saabach, and the other, anonymous, reviewer(s) for their contribution to the peer review of this work. A peer review file is available.

**Reprints and permissions information** is available at <http://www.nature.com/reprints>

**Publisher's note** Springer Nature remains neutral with regard to jurisdictional claims in published maps and institutional affiliations.

**Open Access** This article is licensed under a Creative Commons Attribution-NonCommercial-NoDerivatives 4.0 International License, which permits any non-commercial use, sharing, distribution and reproduction in any medium or format, as long as you give appropriate credit to the original author(s) and the source, provide a link to the Creative Commons licence, and indicate if you modified the licensed material. You do not have permission under this licence to share adapted material derived from this article or parts of it. The images or other third party material in this article are included in the article's Creative Commons licence, unless indicated otherwise in a credit line to the material. If material is not included in the article's Creative Commons licence and your intended use is not permitted by statutory regulation or exceeds the permitted use, you will need to obtain permission directly from the copyright holder. To view a copy of this licence, visit <http://creativecommons.org/licenses/by-nc-nd/4.0/>.

© The Author(s) 2024